

**MICRO AIR BORNE PARTICULATE ANALYZER
(MICROAPA)**

**FINAL REPORT
CONTRACT NO. 03-346**

PREPARED FOR:

**CALIFORNIA AIR RESOURCES BOARD
RESEARCH DIVISION
CALIFORNIA ENVIRONMENTAL PROTECTION AGENCY
1001 I STREET
SACRAMENTO, CALIFORNIA 95814**

PREPARED BY:

**D. A. NIEMEIER, PRINCIPAL INVESTIGATOR
BEELEE CHUA, CO-PRINCIPAL INVESTIGATOR**

**DEPARTMENT OF ENVIRONMENTAL ENGINEERING
UNIVERSITY OF CALIFORNIA
DAVIS, CALIFORNIA 95616**

NOVEMBER 2006

For more information about the ARB's, Research Division's
research and activities, please visit our Website:

<http://www.arb.ca.gov/research/research.htm>

DISCLAIMER

The statements and conclusions in this Report are those of the contractor and not necessarily those of the California Air Resources Board. The mention of commercial products, their source, or their use in connection with material reported herein is not to be construed as actual or implied endorsement of such products.

TABLE OF CONTENTS

Acknowledgements	4
Executive Summary	5
Chapter 1: Background and Research Objectives	6
Background.....	6
Research Objectives & Tasks	7
System Operation Map.....	9
Chapter References.....	9
Chapter 2: Microfabricated Corona Ionizer	10
Device Level: Principles of Operation.....	10
Chapter References.....	28
Chapter 3: Charging And Collection Of Airborne Nanoparticles Using Microfabricated Corona Ionizer	30
Principles of Operation	30
Experimental Setup and Results.....	32
Analysis and Discussion	38
Chapter References.....	39
Additional Readings	40
Chapter 4: Separation Of Airborne Particles Using Microfabricated Corona Ionizer With Integrated Separator Electrodes (Mini-DMA)	41
Introduction	41
Principle of Operation.....	42
Experimental Setup and Results.....	45
References	50
Chapter 5: Particle Sorting Using the Microfabricated Corona Ionizer And Separator Electrodes (Mini-DMA)	51
Device Level Principles of Operation.....	51
Experimental Setup and Procedure	51
Particle Pass-Through-Ratio.....	54
Particle Sorting Results using the Mini-DMA.....	57
Experimental Electrical Mobility of Particles.....	61
Chapter References.....	63
Chapter 6: System Level Integration and Operations	64
System Level Components	64
Controller Board.....	64
Pump and Flow Meter.....	66
High Voltage DC-DC Converter.....	66
Faraday's Cup and Electrometer.....	66
Wireless.....	66
Autonomous Power Supply	66
Potential Extended Capability.....	66
Integrated MicroAPA	68
Conclusion	74
Technology Transfer.....	75

Acknowledgements

The study team would like to acknowledge and thank the following people for their contributions to this research. For aerosol instrumentation: Dr. Mang Zhang, Dr. Yongjing Zhao, Jian Wen, and for microfabrication: Dr Zhihong Li, Dr Wenpin Shih, Dr Daniel McCormick.

Executive Summary

This report describes the design, development, fabrication and testing for primary functionality of an integrated prototype of a small footprint particle size sampler, the MicroAPA. The new instrument consists of a custom designed and fabricated MEMS based ionizer and mini-DMA (separator electrodes), custom designed electrometer and Faraday's cup, as well as off-the-shelf components.

The MEMS based corona ionizer and mini-DMA were constructed using microfabrication techniques. This allows a corona pin diameter of 20 μ m to be easily achieved at a very low cost. It also permits the corona pin to be accurately positioned between two miniature copper grids 4mm apart. By using a high voltage but low current power source, a steady corona discharge is achieved at very low power consumption (less than 20mW). In-lab experiments show that the MEMS based corona ionizer and mini-DMA are able to adequately sort particles ranging from 30nm to 300nm (with the size distribution limited by the TSI constant output atomizer capabilities, which is 30nm to 300nm).

A custom designed electrometer circuit has also been developed by a vendor for the MicroAPA project. The electrometer has a gain of 1V/pA with the baseline voltage at 250mV. A custom designed Faraday's cup consisting of a detection cup nested within shielding cup was also designed and fabricated by the MicroAPA study team. The detection cup captures incoming charged nanoparticles and relays the electrical current to the electrometer.

System integration was based on a super-PLC controller as the main platform. The board controls all data relay and acquisition as well as power management and components algorithms. The integrated prototype was successfully tested in a laboratory environment using an atomizer as the nanoparticle source. It has also been deployed in a controlled roadside environment. These results, while encouraging also suggest that additional modifications to the Faraday's cup are necessary.

In summary, the current instrument specifications and testing show that the prototype instrument design will perform acceptably in protected, indoor environments and with its current chassis, in conditions that range from 40-100 degrees F and RH less than 90 (California weather). For sampling of stacks under high temperature conditions, additional experimentation would be required.

Chapter 1: Background and Research Objectives

Background

In the late 1990's EPA promulgated a new fine particulate matter (PM_{2.5}) air quality annual standard (15 µg/m³) and a 24-hour standard (65 µg/m³). These standards, which are mass-based, are insensitive to even large numbers of ultrafine (diameter < 100 nm) and nanoparticles (diameter < 50 nm). Yet, high numbers of ultrafine and nanoparticles have been found to be correlated with adverse health effects (e.g., 1, 2). Recent epidemiological studies have suggested that exposure to even acute (less than 12 hr) ambient concentrations of ozone (O₃), carbon monoxide (CO), and PM_{2.5} can lead to a range of health problems, including decreased lung function and an increased incidence of respiratory illnesses.

There is a critical need to better characterize the levels of, and micro-environmental conditions leading to elevated short-term personal PM_{2.5} exposure, but in order to do so better pollutant measurement techniques are necessary. Vehicles are major sources of fine particle and currently there are no reliable models available to predict the fine particle size distributions from vehicles, especially under the various modes of vehicle operation (speed, acceleration rate) and the wide range of atmospheric meteorological conditions (temperature, relative humidity) that occur under real-world driving conditions. In general, comprehensive studies of airborne particle effects on climate and human health are hampered by a paucity of instruments that are affordable, portable and easy to maintain, while providing an accurate assessment of the number and size distribution of airborne particles. Fast-response particle sizing instruments capable of capturing the particle distribution under transient vehicle operation modes are commercially available (e.g., Electrical Low Pressure Impactor, ELPI, Dekati Ltd., Finland). However, high costs (approximately \$75,000 and higher), large footprints and insufficient robustness often prohibit simultaneous large-scale, long-term field sampling.

Recent technological advances in hardware design and systems architecture have resulted in a new generation of sensors that are capable of monitoring a range of chemical and physical information. These advances provide an important platform for exploring new and innovative methods for gathering real-time micro-environment data that can significantly increase our understanding of the roadside conditions associated with elevated exposures to PM_{2.5} fine particles.

The purpose of this project was to develop new low-cost micro-scale sensor technology that would allow real-time measurement of fine particulate matter distributions. The new sensor element is based on micro electro-mechanical systems (MEMS) technology, which reduces the footprint and the bulk manufacturing cost and can be coupled with off-the-shelf miniature power supply (both high and low voltages) units, data acquisition modules and air pumps. By developing a new, small footprint, low cost sensor, researchers will be able to deploy and quantify PM_{2.5} number distribution exposure in a various environments, ranging from inside manufacturing plants to busy congested urban

areas where spatially distributed sampling with conventional instruments is not feasible or affordable.

Research Objectives & Tasks

The objective of this project was to employ micro electro-mechanical systems (MEMS) technologies to develop a low cost, portable, reliable prototype microsensor for conducting airborne particulates analysis (MicroAPA). Conventional particle analysis instruments are expensive, bulky, fragile, and unsuitable for spatially distributed, sustained monitoring. With MEMS microfabrication, there is the possibility of major cost reductions over current technologies, thus enabling ubiquitous, continuous sensing. The MicroAPA concept is new and hinges on a MEMS sensor element which was developed during this project. Most other key components such as the high voltage power supply, miniature air pump and data acquisition modules can be procured off-the-shelf.

The proposed project involved a tight coupling between MicroAPA users (researchers from environmental engineering, civil engineering) and device/hardware developers (researchers from electrical engineering and mechanical engineering). Throughout the entire course of the project there were multiple iterations of design, development, testing, and validation.

The specific objectives of the project were:

OBJECTIVE 1. Fabrication of key system devices and prototype configuration.

Using a recently designed and fabricated and successfully tested microfabricated corona ionizer process, we integrated a differential mobility analyzer (DMA) and electrometer probe with the ionizer on a single chip. The chip serves as the sensor element of the MicroAPA.

OBJECTIVE 2. System integration and network testing.

The objective of this task was to integrate the MicroAPA sensor element with its supporting platform of commercially available miniature air pumps, high voltage supply, data logger and control electronics to form a fully autonomous system. Wireless communication and data acquisition modules were incorporated into the system to facilitate networked remote data collection. (Chapters 4 & 5)

OBJECTIVE 3. Prototype evaluation in laboratory and limited field experiments.

We conducted key laboratory evaluation trials and very limited field trials for validation. We conducted a comparison of sensor data to commercial large-scale instruments in terms of temporal and spatial resolution of particle size distributions under fairly controlled operating environments; we evaluated the sensor as a particle collection device under limited real-world sampling conditions, and we examined particle mass collection

on sensor electrometers under various temperature and relative humidity conditions. (Chapter 5)

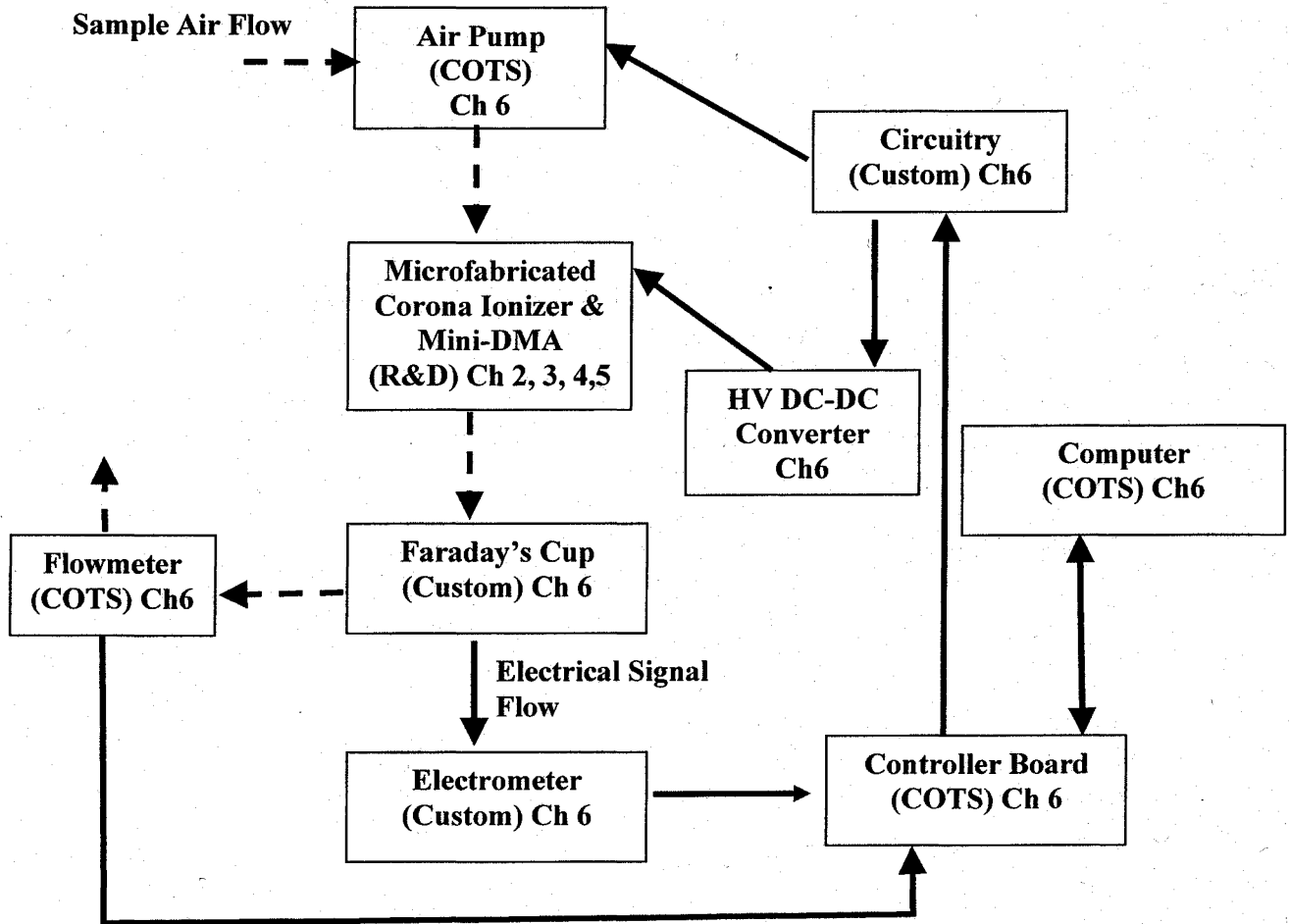
OBJECTIVE 4. Technology Transfer.

The objective of this task was to establish the linkage between prototype development and full-scale production. As part of this effort, we submitted a right of invention and participated in the Little Bang contest which links campus researchers to venture capitalists. This report, which contains the technical specifications for the design of the MicroAPA will also be open-sourced.

MicroAPA Systems Operation Map (Next page).

In the MicroAPA, ambient air is first drawn into the apparatus as sample air via the air pump. The sample air passes over the micro ionizer where the airborne particles are electrically charged. The charged particles moved into the mini-DMA where they are sorted according to electrical mobilities. Only particles with lower electrical mobilities are passed into the Faraday's cup for detection. The Faraday's cup captures incoming charged particles and the electrical charges on the particles are collected. This translates to a small electric current that is amplified by the electrometer. The readout from the electrometer corresponds to the number of the particles trapped by the Faraday's cup. The HV DC-DC converts low voltages to high voltages to power the micro ionizer and mini-DMA. The flow meter provides feedback on the flow rate passing through the apparatus. The controller board controls all components on board the MicroAPA.

System Operation Map



Chapter References

1. Schwartz J, Dockery D, Neas L. 1996. *J. Air Waste Manage. Assoc.* 46(927-39)
2. Oberdorster G, Gelein R, Ferin J, Weiss B. 1995. *Inhalation Toxicology* 7(111-24)

Chapter 2: Microfabricated Corona Ionizer

A major technological innovation employed in the MicroAPA is a microfabricated corona ionizer and mini-DMA. Microfabrication involves manufacturing techniques that are commonly used in the integrated circuits industry. It allows devices with very small features to be fabricated in bulk and at low cost.

As part of this research effort, a microfabricated corona ionizer was constructed consisting of a tiny needle, 5 μ m in width, centered between two parallel plates spaced at 1mm apart. The corona ionizer is set in an air channel of 1mm by 2mm. By applying a high voltage between the pin and the parallel plates, a corona discharge is intercepted at the tip of the pin. The subsequent generated electron cloud drifts away from the tip of the pin and charges airborne particles that come in contact with it. As of the writing of this report, this is the smallest corona ionizer with a demonstrated ability to charge airborne particles.

The corona ionizer consumes less than 20mW of power during operation. It requires a voltage of about 2kV at a current of few tens of microamperes. This high voltage is provided by commercial off-the-shelf (COTS) high voltage dc-dc converter. Using photolithography and electroplating techniques, both the corona ionizer and parallel plates are manufactured on the same glass substrate. Airborne particles charged by the corona ionizer are passed into the parallel plates (known as separator electrodes or mini-DMA, see Chapter 4) to be sorted in accordance to their electrical mobilities. Sorted airborne particles exit into a Faraday's cup where their electrical charges are measured as electrical current. Due to the small magnitude of the current, an electrometer is used to amplify the current.

The footprint of the corona ionizer is no more than 1cm x 1cm and the combined footprint is about 1cm by 3cm, with a thickness of 3mm. This provides the basis for a small footprint and low power sensor that can be deployed autonomously.

Device Level: Principles of Operation

The primary operational environment of the microfabricated corona ionizer is in gases at atmospheric pressure and composition. D.C. corona discharge at atmospheric conditions requires the Townsend avalanche to be confined at the surface of the discharge electrode. This is commonly achieved using highly electrically stressed electrode pairs of specific geometries to create a large asymmetry in the Laplacian electric field distribution. Common geometries include pin-to-plane, wire-to-plane and wire-in-cylinder. A sufficiently large field magnitude sets off an avalanche of carriers while a large electric field gradient prevents the avalanche head from extending beyond the vicinity of the discharge electrode. The electrons are constantly replenished by secondary processes such as extraction of secondary electrons from cathode by ion bombardment or incident by photons. These secondary processes enable the discharge to be self-sustaining without the need for an external ionizing agent such as UV rays.

The magnitude of the electric field gradient between the electrodes is critical in sustaining a corona discharge over a wide voltage range. The larger the magnitude of the electric field gradient, the larger the corona discharge operating voltage range before it develops into brush discharge and sparkover. A brush discharge or sparkover occurs when the avalanche head crosses the gap between the electrodes. This occurs when electric field strength between the electrodes is sufficiently large for the Townsend avalanche to continue beyond the surface of the discharge electrode. In the absence of sufficient electric field gradient, a sparkover or brush discharge occurs without the prior appearance of the corona [1].

D.C corona discharge can be either positive or negative. Negative D.C. corona discharge is chosen for the particular application because it promotes stable operation as the γ effect (depends only on cathode material and gas composition) dominates over other secondary electron replenishment processes such as β , δ and η effects [2]. It also has a stable current-voltage characteristic for a wide range of orthogonal airflow velocities across the drift region. This implies that in a pin-to-plane configuration, the pin serves as the cathode (negatively biased) while the plane becomes the anode (positively biased). For circuitry simplicity, the anode is often grounded.

The key charging mechanism is performed by the cloud of electrons resulting from the avalanche process near the cathode surface. These electrons do not possess sufficient energy to perform further impact ionization as they move towards the anode due to the decreasing electric field gradient. As a result, the electrons attach themselves to electronegative gas molecules and particles that pass through the drift region, thus completing the charging process. Figure 2.1 shows the schematic of a corona ionizer and the corresponding charging process.

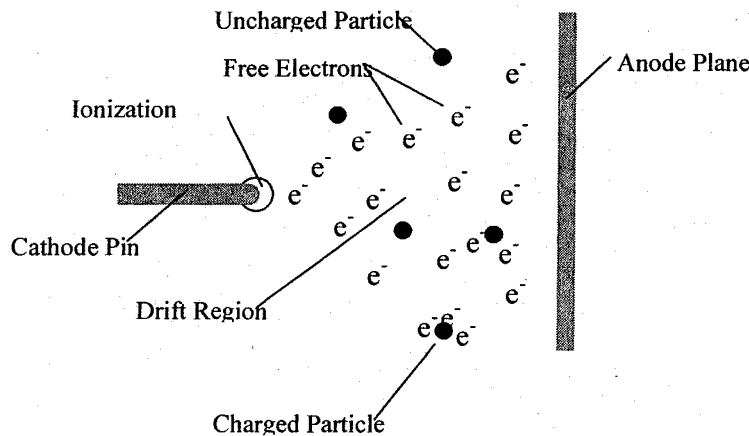


Figure 2.1: Schematic of a negative corona discharge ionizer and the corresponding charging process.

Breakdown Criterion and Figure-of-Merit for Self-Sustaining Discharges

There have been numerous investigations to determine the inception voltage for the onset of a corona discharge [3]. Notably, Peek [1] has arrived at a now-well-known empirical equation for the surface electric field strength of electrodes to initiate a visual corona for both wire-to-wire and wire-in-cylinder configurations. This equation is known as the Peek's breakdown criterion and it is given as follows:

$$E_{Critical} = A\delta \left(1 + B\sqrt{\frac{\delta}{r}} \right) \quad (2.1)$$

r is the tip radii of curvature of the electrode whose surface the ionization will first take place; δ is the relative air density given by T_oP/TP_o where T_o and P_o are the reference temperature of 293K and reference pressure of 1 atm (760 Torr), respectively, and T and P are the temperature and pressure at which the ionization takes place. Both A and B are coefficients derived empirically and they are commonly given as approximately 30 kV/cm and $0.3 \text{ cm}^{1/2}$, respectively. Equation 2.2 shows a modified version of the criterion where the surface roughness of the electrodes is considered as well.

$$E_{Critical} = Af\delta \left(1 + B\sqrt{\frac{\delta}{r}} \right) \quad (2.2)$$

f is given as 1 for smooth surfaces ($f = 0.6$ for most applications) and $E_{Critical}$ increases with humidity [4]. The significance of Equations 2.1 and 2.2 will be discussed further in the next section where design considerations are presented.

Another figure-of-merit that is commonly used to describe the breakdown criterion for self-sustaining discharge is the E/N ratio where E is electric field strength and N is the gas number density. The ratio can also be expressed as E/P where P is the gas pressure. Qualitatively, it describes the amount of energy possessed by the carrier or molecule. The unit of E/N is *townsend* or Td, where 1 Td is 10^{-17} Vcm^2 . The characteristic E/N value for plane parallel electrodes in air at atmospheric conditions is about 120 Td [3].

A similar figure-of-merit is given in the Paschen's Law [5] where it is also commonly used to estimate the breakdown voltage. In this case, the breakdown voltage is a function of the product of the gas pressure p and the gap distance between the electrodes d . Hence the product pd is used as the figure-of-merit whenever Paschen's Law is invoked. The original experiment by F. Paschen during the 19th century was carried out using spherical conductors in ambient air. Since then numerous similar experiments have been performed by others to arrive at "Paschen Curves" for other electrode geometries and with different gases. It is important to note that Paschen's Law is not useful for predicting breakdown voltages for high pressures, very small electrode spacing [6, 7] and inhomogeneous fields [7].

The breakdown criterion can also be described based on Townsend electron avalanche theory. Coefficients are used to indicate the mechanisms as well as the number of ions or electrons generated by a single electron. One such coefficient is known as the first Townsend coefficient given by α . It represents the mean number of pairs of ions formed by an electron per unit distance [2]. It is also sometimes given as the difference between

the primary ionization and attachment coefficients [8]. Other known coefficients used as are follows:

- (i) β : represents ionization by positive ions that were created by the initial electron.
- (ii) γ : represents emission of secondary electrons via the ions impaction of the cathode.
- (iii) δ : represents emission of secondary electrons via the photons impaction of the cathode.
- (iv) ε : represents emission of secondary electrons via the excited metastable atoms impaction of the cathode.
- (v) η : represents photo-ionization effect.

The general form of Townsend breakdown criterion [2,8] can be written as

$$C \left(\exp \left(\int_0^d \alpha dx \right) - 1 \right) = 1 \quad (2.3)$$

Where d is the electrode gap spacing, x is the axis, and C , which is also known as the second Townsend coefficient, is given as:

$$C = \gamma + \frac{\beta + \delta + \varepsilon + \eta}{\alpha} \quad (2.4)$$

In the case of a negative D.C. corona discharge, Townsend breakdown criterion is dominated only by α and γ . The breakdown criterion is therefore simplified to:

$$\gamma \left(\exp \left(\int_0^d \alpha dx \right) - 1 \right) = 1 \quad (2.5)$$

It is useful to give a brief description of the events that follow after the initial breakdown or avalanche. This is given in the context of a self-sustaining discharge. Upon the fulfillment of the Townsend breakdown criterion, a Townsend discharge will develop. This means there is a series of self propagating avalanches without perturbation to the Laplacian electric field distribution. The subsequent increase in the electrical current will result in the transition into a glow discharge. This is characterized by the localized distortion of the Laplacian electric field distribution at the vicinity of the ionization zone by the space charge that has been formed. The glow discharge can be sustained at a lower voltage than the Townsend discharge. As the current increases, often due to an increase in the voltage, thermionic emission at the cathode becomes the dominant secondary electrons replenishment process and an arc develops. The electric field distribution in an arc is completely distorted. It is also possible to develop an arc without first having a Townsend or glow discharge.

Design Considerations

The two main steps that lead to a corona discharge can be describes as follows: (i) the initiation of Townsend avalanche (ii) the sustenance of the avalanche and confining it to

the surface of the discharge electrode without it crossing the electrodes' gap. The challenges in designing a microfabricated corona ionizer are as follows:

- (a) The electrical insulation of the substrate between the electrodes must withstand high electrical field strength (up to several tens of kV/cm) prior to the initiation of Townsend avalanche.
- (b) The initiation of the avalanche and the subsequent discharge must only occur at the surface of the discharge electrode. Undesirable discharges at other locations must be prevented. For example, it cannot occur at the corners of the anchors, routing and electrical contact pads.
- (c) Designing the geometries of the electrodes such that the electric field gradient is sufficiently large to sustain a wide operating corona voltage.
- (d) Minimize the effect of the discharge electrode wear due to sputtering and evaporation during the discharge process.
- (e) Packaging of the ionizer must withstand high voltages.

The desired specifications of the microfabricated generic corona ionizer are as follows:

- (i) A footprint of approximately 1cm^2 with a device height of approximately 1mm.
- (ii) An operating corona voltage of less than 3 kV (commercial-off-the-shelf power supply available in small packages).
- (iii) An operating corona voltage range of few hundred volts (for stability of operation and wide range of operation).
- (iv) An operating corona current of more than $1\ \mu\text{A}$.

To address the above mentioned challenges and specifications, the chosen device topology uses electroplated copper structures on glass. Glass is an excellent electrical insulator and is able to withstand an electrical potential difference of several kilovolts. It has a dielectric constant of at least 3.8 and can be as high as 14.5. Using a pin-to-plane configuration, each electrode has supporting structures consisting of the anchor, the routing and the electrical contact pad. This topology allows the electrodes and their supporting structures to be laid out in-plane on the substrate. It is relatively easy to position the pin and the plane such that they are in close proximity to each other as compared to other supporting structures. This will prevent undesirable discharges at other locations on the supporting structures.

Surface wear of electrodes due to sputtering and evaporation is not a significant issue since the electrodes are entirely made of copper. In comparison, previously reported ionizers used a thin film of metal as the conducting surface. The thin film of metal is easily worn off by sputtering and evaporation during the discharge [9-11].

Estimation of the Electrodes' Geometrical Dimensions

In a pin-to-plane configuration, three geometrical parameters determine the magnitude of the electric field gradient. The three geometrical parameters are the radius of curvature of the pin r , the electrode gap d and the width of the plane l . Figure 2.2 shows the geometrical parameters of the pin-to-plane configuration.

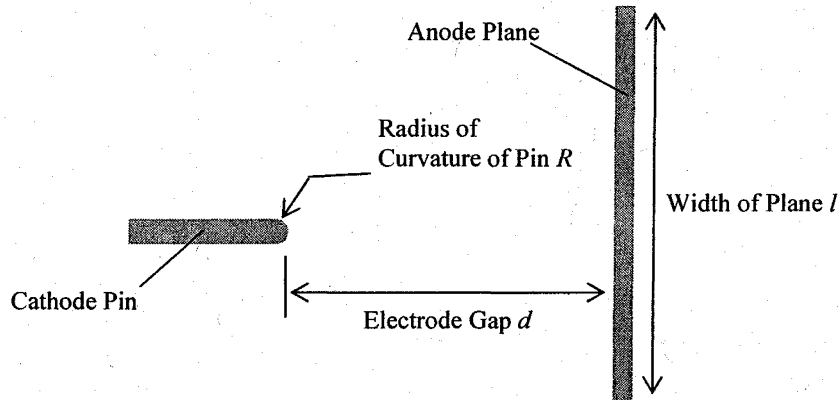


Figure 2.2: Schematic of geometrical parameters of pin-to-plane configuration.

Assuming l is large compared to r and d , it is desired to have the ratio r/d be as small as possible to maximize the magnitude of the electric field gradient. The lower bound for r is determined by the minimum feature size of the fabrication process (after electroplating) which conservatively estimated at $20\mu\text{m}$. The upper bound for d is constrained by the maximum allowable voltage (3 kV) in order to develop the required electric field strength for inception.

Determination of d for Initial Discharge Inception

Possible values for d have to satisfy the first step (initiation of Townsend avalanche) required for a corona discharge. The three breakdown criteria (Peek's, Paschen's and Townsend's) are useful for this purpose with varying degree of convenience for analytical purposes. It is important to note that these three breakdown criteria are similar in principle and do have certain consistencies among themselves. Townsend's criterion requires the geometrical characteristics of the ionizer design to be reflected in the first and second coefficients. Paschen's Law is more commonly represented as Paschen's Curves for specific discharge setups. Peek's breakdown criterion is represented in an empirical equation with coefficients corresponding to various electrodes' geometries and physical conditions. It is not clear that any of the above criteria gives a relatively more accurate representation since they are either based on ideal operating conditions or empirically-derived coefficients. However Peek's breakdown criterion is of a relatively more convenient form to be used for our purposes.

For the initiation of the Townsend avalanche, the surface electric field strength of the pin has to be equal or larger than the Peek's breakdown electric field strength as given by

equation 2.2. The inception voltage is calculated by setting the geometrical electric field strength equal to the Peek's breakdown electric field strength. Unfortunately the coefficients for equation 2.2 are only available for three specific electrodes configurations, namely: (i) wire-in-cylinder, (ii) parallel wires and (iii) spheres of identical radius. Therefore it is unclear that it is accurate to apply these coefficients for the pin-to-plane configuration. On the other hand, the pin-to-plane configuration may be approximated with similar configurations using the same characteristic length, which in this case is the radius of the pin, sphere or wire.

The maximum electric field strength of a pin-to-plane configuration [7, 8] is given as follows:

$$E_{pin-to-plane} = \frac{2V}{r \ln \left[\left(\frac{2d}{r} \right) + 1 \right]} \quad (2.5)$$

Where E is the electric field strength, V is the voltage between the pin and plane, r is the radius of curvature of the pin and d is the gap distance between the pin and the plane. To calculate the values of the inception voltage $V_{inception}$, the maximum electric field strength of the configuration $E_{pin-to-plane}$ is set equal to the critical electric field strength (given by Peek's breakdown criterion) as follows:

$$E_{pin-to-plane} = E_{critical} \quad (\text{As given in equation 2.2}) \quad (2.6)$$

$$\frac{2V_{inception}}{r \ln \left[\left(\frac{2d}{r} \right) + 1 \right]} = 30 f \delta \left(1 + 0.3 \sqrt{\frac{\delta}{r}} \right) \quad (2.7)$$

Assuming $f=1$ and $\delta=1$, Equation 2.7 can be rewritten as:

$$V_{inception} = 15r \left(1 + \frac{0.3}{\sqrt{r}} \right) \ln \left[\left(\frac{2d}{r} \right) + 1 \right] \quad (2.8)$$

Similar operation can be performed for three other configurations namely: wire-in-cylinder, wire-to-plane and sphere-to-plane to calculate the respective $V_{inception}$.

For wire-in-cylinder:
$$V_{inception} = 30r_{wire} \left(1 + \frac{0.3}{\sqrt{r_{wire}}} \right) \ln \left(\frac{r_{cylinder}}{r_{wire}} \right) \quad (2.9)$$

For wire-to-plane:
$$V_{inception} = \frac{30d \left(1 + \frac{0.3}{\sqrt{r_{wire}}} \right)}{0.25 \left(\frac{d}{r_{wire}} \right) + 1} \quad (2.10)$$

For sphere-to-plane:

$$V_{inception} = \frac{30d \left(1 + \frac{0.3}{\sqrt{r_{sphere}}} \right)}{0.94 \left(\frac{d}{r_{sphere}} \right) + 0.8} \quad (2.11)$$

Since Peek's breakdown criterion is based on empirical results using an inter-electrode gap in the order of 1mm or more, the range of values used for d in the calculation of $V_{inception}$ will also be limited to similar magnitude range. This will, at the minimum, ensure meaningful results from the computation using the wire-in-cylinder configuration. Figure 2.3 shows the results of the computation using values of d from 0.1mm to 2mm. The value of r used for the computation is $20\mu\text{m}$ (conservative estimate based on the fabrication process). As shown in Section 5.8, the inception voltage is a weak function of r for values less than $200\mu\text{m}$. The value of the relative air density δ used in the computation is 1. Recall that δ given by $T_o P / T P_o$, where T_o and P_o are the reference temperature of 293K and reference pressure of 1 atm (760 Torr) respectively. A smooth wire/pin surface is assumed ($f = 1$) to ensure that the computed inception voltage is an upper bound value. With the availability of subsequent experimental measurements, the value of f can be determined.

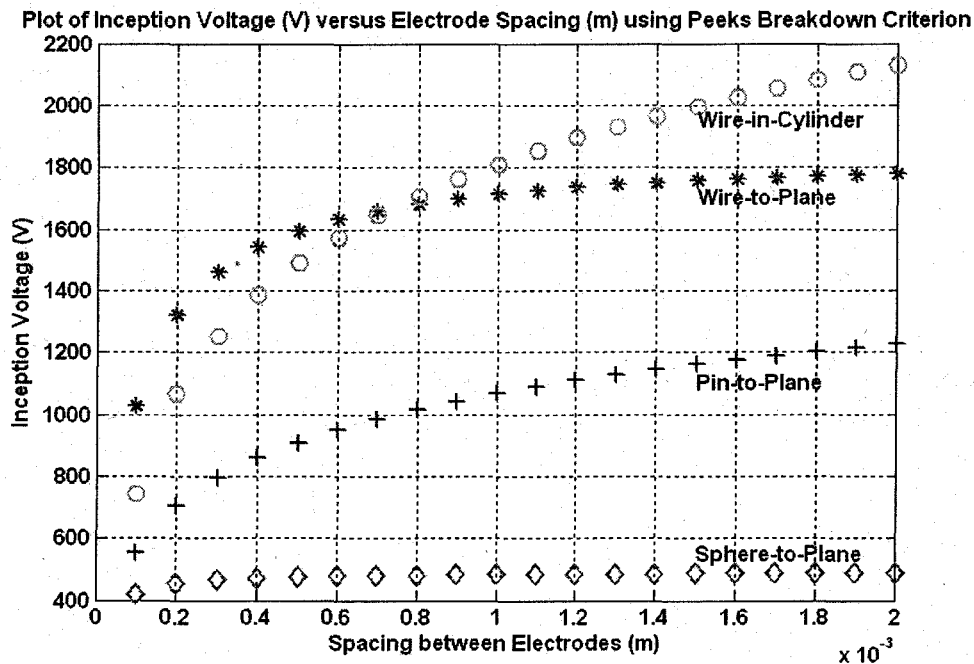


Figure 2.3: Plot of Inception Voltage (V) versus Electrode Spacing (m) using Peek's Breakdown Criterion for various electrode configurations.

From Figure 2.3, the computation results for both wire-to-plane and sphere-to-plane shows little dependency on the electrode spacing as the value of the spacing gets larger. It can also be seen from equations 2.10 and 2.11 whereby the dependency on the spacing d

ceases to be dominant as it becomes significantly larger than the radius of the wire and sphere respectively. This brings forth the question of appropriateness in using the empirical electrostatic field expressions for both wire-to-plane and sphere-to-plane with large spacing-to-radius ratios in the computation. Nevertheless, it does not necessarily nullified the results, especially that for the wire-to-plane configuration. This is because the coefficients for the Peek's breakdown criterion used in the computation are for a similar wire-in-cylinder configuration. The values of $V_{inception}$ calculated for these two configurations are less than 2 kV for an electrode gap spacing of 2mm.

For the pin-to-plane configuration, $V_{inception}$ is less than 1.3 kV for an electrode gap spacing of 2mm. Even though Peek's breakdown criterion coefficients used in the computation are derived from a different (wire-to-plane) configuration, the result is still useful for giving an indication of the order of magnitude for $V_{inception}$.

Finally, for the wire-in-cylinder configuration, a $V_{inception}$ is 2.1 kV at an electrode gap spacing of 2mm. The value of $V_{inception}$ computed is accurate as it uses coefficients derived from the same configuration. The result is useful as the configuration approximates that of pin-to-plane for a small wire radius.

It is also apparent from Figure 2.3 that the voltage increases with decreasing electric field asymmetry. This is consistent with the understanding that the same surface electric field strength is to be attained for all four configurations since the same Peek's breakdown criterion coefficients are used.

In summary, the approximated computations indicate the required $V_{inception}$ for d at values around 2mm is less than 3 kV, thus fulfilling the design specification for inception.

Values of l required for a Corona Discharge

Fulfillment of the breakdown criterion alone does not assure the occurrence of a corona discharge. It is possible for the initial breakdown to develop into an arc without first having a corona discharge if the electric field gradient is not sufficiently large. Therefore suitable values for l are required to ensure sufficiently large electric field gradient for a corona discharge. Warburg's Law [12-14] provides a convenient geometrical estimate for the value of l (for a given value of d). Warburg's Law is originally used to describe the current density distribution in a pin-to-plane corona discharge configuration. It indicates the boundary of the current circle on the plane for a given electrode gap spacing. The current circle is also indicative of the desired plane area for a corona discharge. Figure 2.4 shows the schematic of the pin-to-plane configuration and its corresponding current circle.

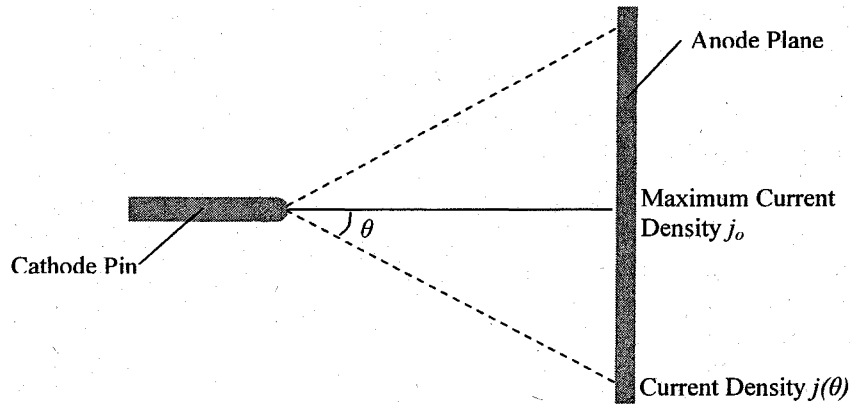


Figure 2.4: Schematic of pin-to-plane configuration and its corresponding current circle subtended by angle θ where j is the current density arriving at the anode plane.

Warburg's Law gives the current density distribution at the plane as a function of the angle θ . The experimentally measured maximum current density is given by j_0 . The spatially dependent current density j is given as:

$$j = j_0 \cos^m \theta \quad (2.12)$$

where $m = 4.65$ for a negative discharge. As θ becomes larger than 60° , value of j rapidly approaches zero.

In absence of spatially dependent electric field strength profile computation, $\theta = 60^\circ$ can be used with a known value of d to compute the required value for l as given below:

$$l = 2d \tan \theta \quad (2.13)$$

Therefore using $d = 2\text{mm}$ as calculated previously, l is calculated as approximately 3.5mm.

Design Layout

Using the values of $r = 20\mu\text{m}$, $d = 2\text{mm}$ and $l = 3.5\text{mm}$ as an approximate geometrical guideline, the corona ionizer design is implemented using an electroplating based microfabrication process. Figure 2.5 shows the schematic of the corona ionizer.

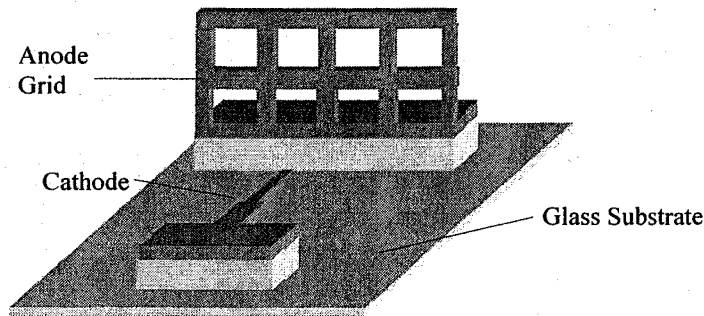


Figure 2.5: Schematic of microfabricated corona ionizer.

The plane is replaced with a grid to facilitate the fabrication process. In the earlier computations, the height of the plane is assumed to be same as the width of the plane l . However due to the limitation of the fabrication process, the height of the plane only has a value as large as that of d . Nevertheless it is not an issue since both l and d have similar values. Figure 2.6 shows the layout schematic of the corona ionizer.

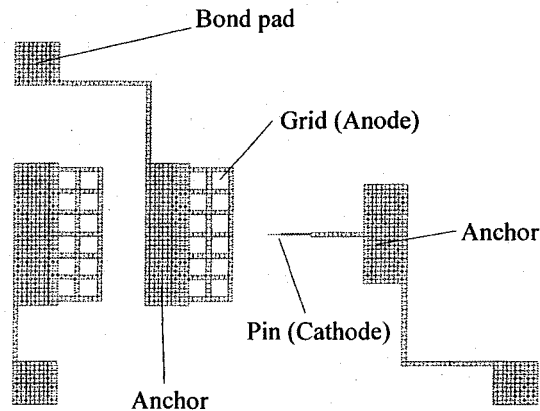


Figure 2.6: Layout schematic of corona ionizer.

The geometrical dimensions of the corona ionizer are shown in Table 2.1. The suspension height refers to the gap between the suspended pin and the glass substrate. The thickness

of the cathode is also the overall structural thickness achieved after the electroplating process.

Table 2.1: Table of Geometrical Dimensions of Corona Ionizer

Suspension Height	~300 μm	Cathode Primary Width	~20 μm
Anode Grid Width	7mm	Cathode Secondary Width	~100 μm
Anode Grid Height	1.1mm	Cathode Thickness	~20 μm
Cathode Length	2.8mm – 3.6mm	Inter-electrode Spacing	1.4mm – 2.2mm

Fabrication

We use a single mask fabrication process that begins with the deposition of 1500 angstroms of copper (on top of 100 angstroms of titanium for adhesion) on a glass substrate as electroplating seed layer. Approximately 1.5 μm of Shipley 1813 photoresist is used as the electroplating mold. The photoresist thickness is inconsequential since the sidewall profile and cathode width is not critical to the operation of the device. Copper plating is carried out using standard solution with a current density of approximately 33.8mA/cm². The final electroplated thickness is approximately 20 μm . The photoresist mold is stripped and the seed layer is removed in aqueous copper etch. Aqueous hydrofluoric acid is used to remove the titanium seed layer as well as to perform the undercutting of the cathode and anode grid. Manually positioning the released anode grid into vertical alignment by compliance completes the fabrication process. Figure 2.7 shows the schematic of the fabrication process flow.

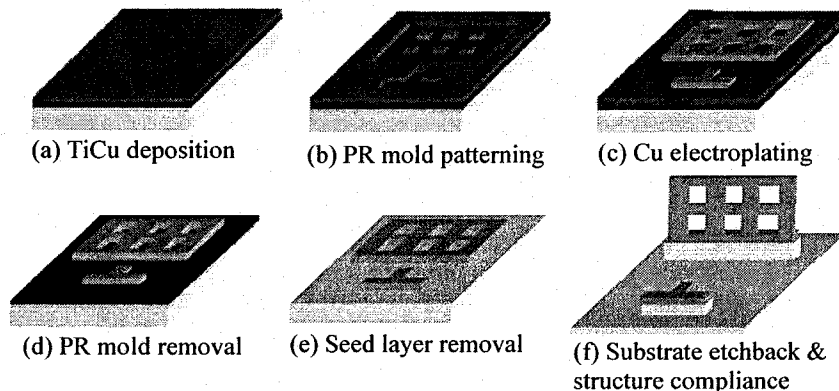


Figure 2.7: Fabrication process flow.

The positioning of the anode grid can also be performed using parallel self-assembly technique based on solder reflow tension forces [15], making it viable for batch manufacturing. This technique can be integrated with the fabrication process with an additional mask layer. Figure 2.8 shows the completed microfabricated corona ionizer.

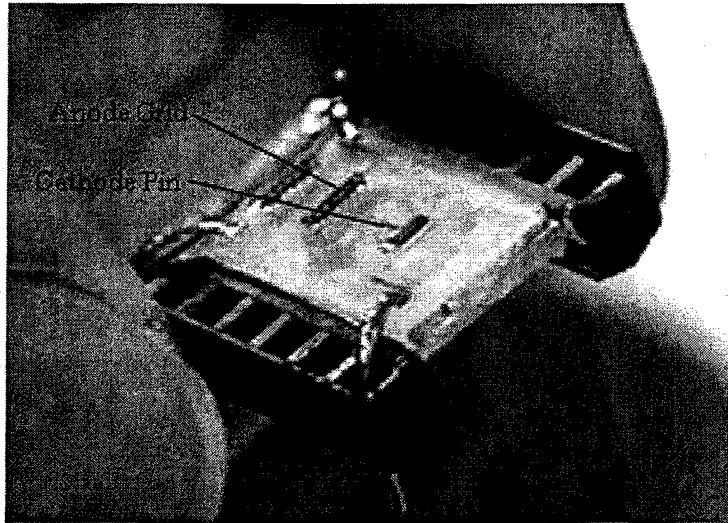


Figure 2.8: Packaged microfabricated corona ionizer.

Experimental Setup and Results

The experimental setup consists of a ZIF (zero insertion force) socket in a grounded aluminum sheath case with high voltage applied via an external power source. The device is custom packaged and inserted in the socket during the test. Humidity and temperature is monitored via sensor probes positioned near the device. The applied voltage is gradually increased until a current change is observed, signifying inception. Inception can also be verified by visual observation of the characteristic blue glow around the cathode as shown in Figure 2.9.

Devices with inter-electrode spacing of 1.4mm, 1.8mm, 2.0mm and 2.2mm were tested. Negative corona discharge was incepted successfully in all devices. Figure 2.10 shows the respective experimental current-voltage plots that correspond to the various inter-electrode spacing at relative humidity of $40\pm 2\%$ and temperature $22\pm 2^\circ\text{C}$. A corona charging current of more than $40\mu\text{A}$ was achieved prior to streamer breakdown. This corresponds to a power consumption that is less than 150mW.

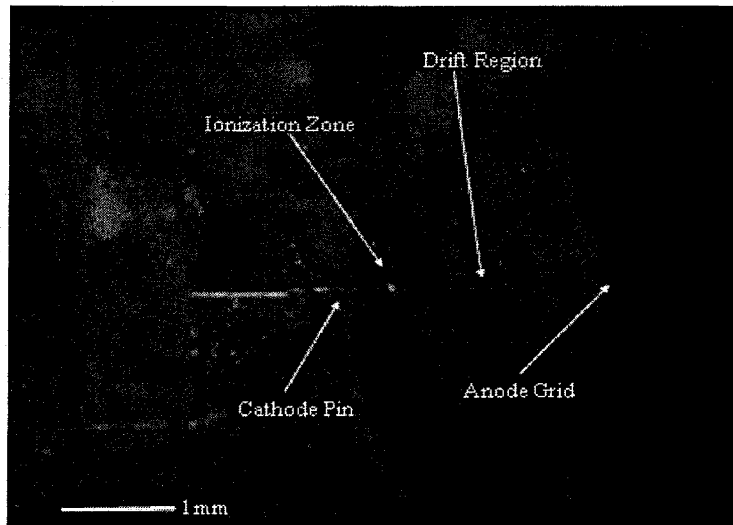


Figure 2.9: Microfabricated corona ionizer in operation.

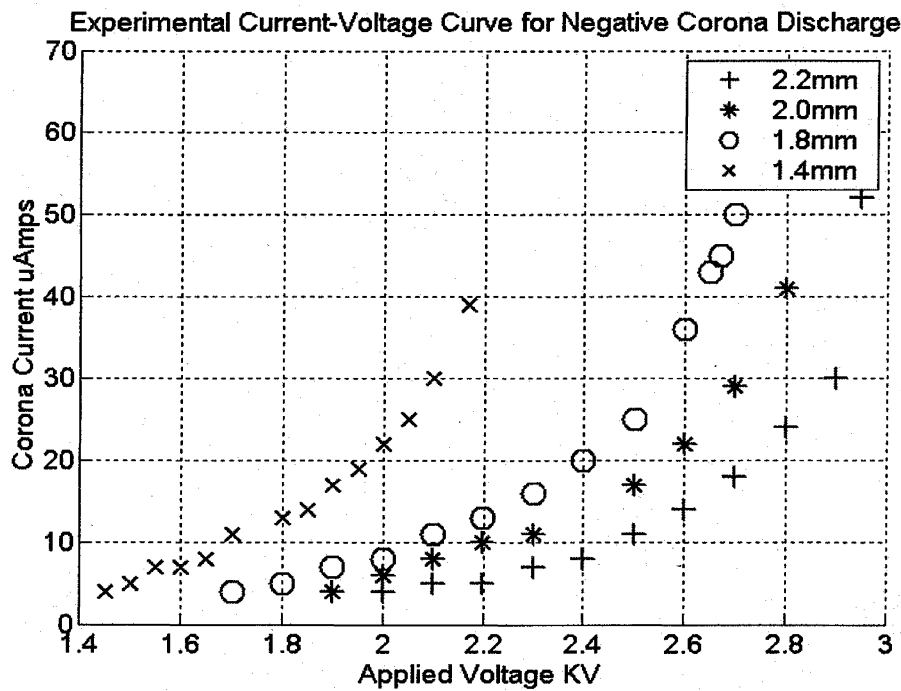


Figure 2.10: Experimental current-voltage plots for various inter-electrode spacing.

The terminating point of each plot indicates the transition from a corona discharge to a streamer breakdown as shown in Figure 2.11. During the onset of the streamer breakdown, a sudden increase in the discharge current by an order of magnitude is

observed. This is because the conductive column formed during streamer breakdown [16] is more efficient in transporting charges than the drift region during corona discharge.

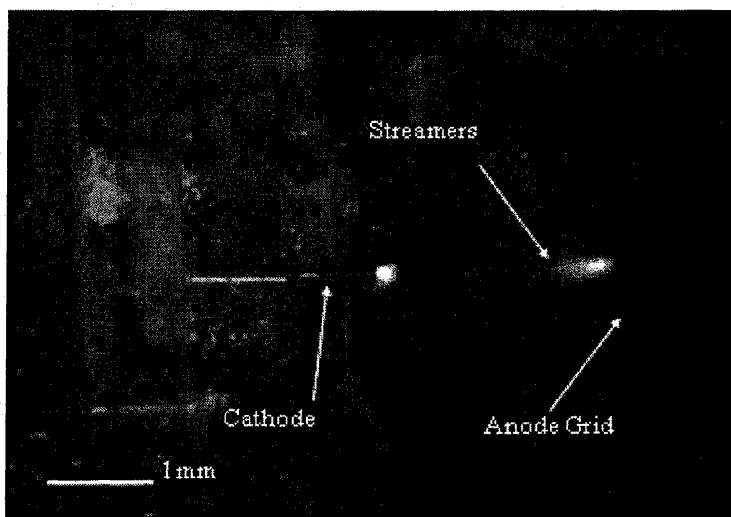


Figure 2.11: Streamers onset at the end of the corona discharge regime.

The streamers extended from the grid into the original corona drift region. This is undesirable for the charging of airborne particles as it results in bipolar charging, thus significantly reducing the number of charges per particle.

The experimental inception voltages are compared with the previously obtained inception voltages as shown in Figure 2.12. The experimental inception voltages are in close agreement with those calculated using wire-in-cylinder and wire-to-plane. The discrepancy is probably due to inaccuracies introduced by using a different configuration in the calculations. It can also be possibly due to the difference between the radius of curvature used for calculation and the effective radius of curvature in the actual device. Nonetheless, this has demonstrated the effectiveness of the method of calculation to estimate the inception voltages for the device.

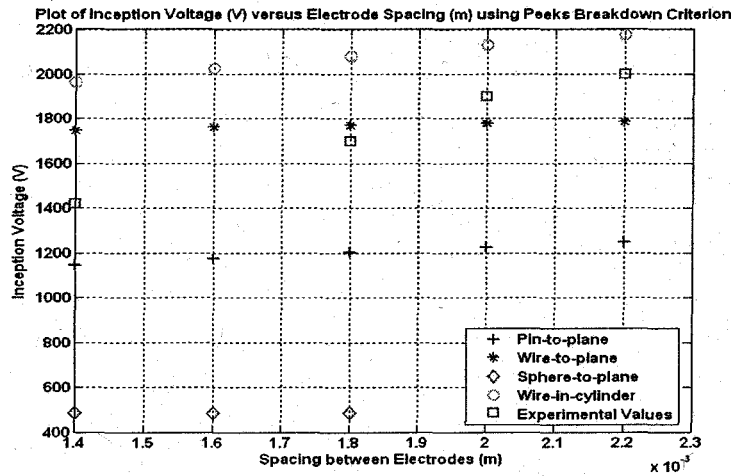


Figure 2.12: Comparison of experimental inception voltages with earlier calculations.

Dual cathode device with an inter-electrode spacing of 2.2mm was also investigated. It has a higher inception voltage of 2.1 kV than that of the single cathode design. This is due to the reduction in the asymmetry of electric field distribution while the cathode surface field strength required for breakdown remains the same. Figure 2.13 shows ANSYS™ electrostatic simulation for both single and dual cathode design for the same inter-electrode spacing and applied voltage. Maximum surface field strength induced by dual cathode design is approximately 20% less than that of the single cathode design, implying a higher inception voltage.

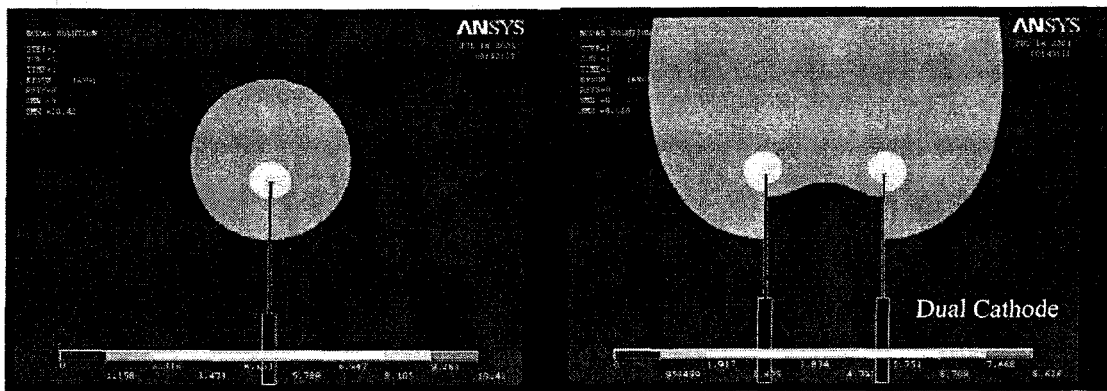


Figure 2.13: ANSYS™ electrostatic simulation of the single and dual cathode designs.

Figure 2.14 shows experimental current-voltage curves for both single cathode and dual cathode design with inter-electrode spacing of 2.2mm. The dual cathode design delivers approximately 4 times more charging current at 2.3kV. The ability to operate with multiple cathodes provides flexibility in adapting the ionizer structure for varying charging loads.

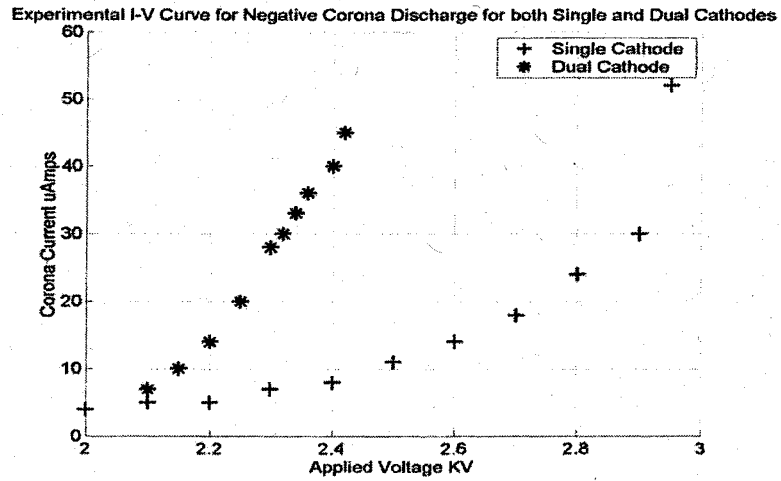


Figure 2.14: Measured corona current-voltage (I-V) curves for both single and dual cathode design.

The experimentally obtained inception voltages are used to establish the cathode surface field strength or voltage gradient electrostatic model in ANSYS™. For each set of inter-electrode spacing, the cathode surface field strength is obtained using an applied voltage that corresponds to the respective inception voltage. The simulation is repeated for varying cathode radii of curvature from 0.5 μm to 200 μm to include the possible values for the effective cathode radii of curvature of the fabricated devices. Figure 2.15 shows the plot of the maximum surface field strength versus the cathode radii of curvature.

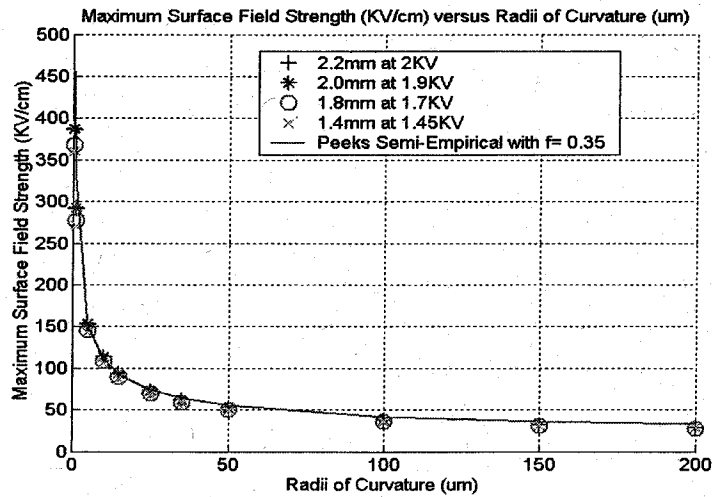


Figure 2.15: Plot of maximum surface field strength versus cathode radii of curvature.

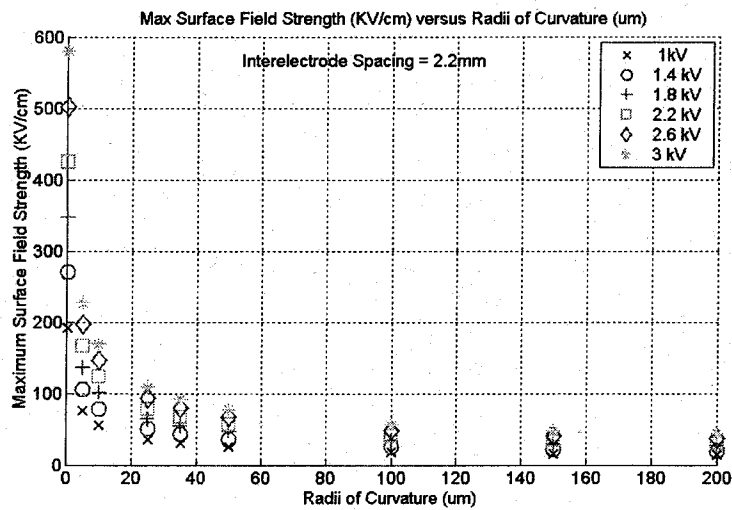


Figure 2.16: Plot of maximum surface field strength versus radii of curvature for a fixed inter-electrode spacing of 2.2mm.

All the plots that correspond to the respective inter-electrode spacing coincide with each other, indicating common radii of curvature between them. In addition, Peek's semi-empirical curve fits closely over the plots using $f = 0.35$. It is reasonable to use $f = 0.35$ because the surface roughness generated by the electroplating process at the pin is not well controlled. This results in a higher relative surface roughness as compared to the

radius of curvature of the pin. Since the value for the maximum surface field strength is unique for a given inter-electrode spacing, pin's radius of curvature and applied voltage as shown in Figure 2.16, we experimentally verified that for a given inter-electrode spacing, the inception voltage is a very weak function of the pin's radius of curvature for large values. The dependence of the inception voltage on the pin's radius of curvature increases as the value of the pin's radius of curvature decreases. This dependence characteristic maybe explained via equation 2.10.

The scaling down of the electrodes' dimensions for microfabrication will not reduce the initiation voltage significantly. In order to maintain the electric field gradient that is necessary for a corona discharge, the discharge electrode's radius of curvature has to be reduced as well. According to Peek's breakdown criterion, higher electric field strength is required for the avalanche initiation for a reduced radius of curvature. Therefore at a given electrode gap distance, the reduction of the electrode's radius of curvature may not bring about a decrease in the applied voltage required for avalanche initiation.

Chapter References

- [1] F. W. Peek, *Dielectric Phenomena in High Voltage Engineering*, McGraw-Hill, 1929
- [2] R. Papoular, *Electrical Phenomena in Gases*, American Elsevier Publishing Company, 1965
- [3] J. J. Lowke, "Theory of electrical breakdown in air-the role of metastable oxygen molecules", *J. Phys. D: Appl. Phys.*, 25 (1992), pp. 202-210
- [4] Y. Zebboudj and R. Ikene, "Positive corona inception in HVDC configurations under air density and humidity conditions", *Eur. Phys. J. AP.*, 10 (2000), pp. 211-218
- [5] F. Paschen, *Wied. A*, Vol 37, 1889, pp. 69
- [6] J. M. Torres and R. S. Dhariwal, "Electric field breakdown at micrometer separations", *Nanotechnology*, 10 (1999), pp. 102-107
- [7] N. Spyrou, R. Peyrou, N. Soulem and B. Held, "Why Paschen's law does not apply in low-pressure gas discharges with inhomogeneous fields", *J. Phys. D: Appl. Phys.*, 28 (1995), pp. 701-710
- [8] M. Goldman and A. Goldman, *Corona discharges Gaseous Electronics*, ed M.N. Hirsh and H. J. Oskam, Academic Press, 1978
- [9] J.C.T Eijkel, H. Stoeri and A. Manz, "A molecular emission detector on a chip employing a direct current microplasma", *Anal Chem.*, Vol. 71, No. 14, 1999, pp. 2600-2606
- [10] R. G. Longwitz, H. van Lintel and P. Renaud, "Study of micro-glow discharges as ion sources for ion mobility spectrometry", *J. Vac. Sci. Technol., B*, Vol. 21, No. 4, Jul/Aug, 2003, pp.1570-1573
- [11] R.G. Longwitz, H. van Lintel, P. Renaud, "Study of micro glow discharges as ion sources", *29th EPS Conference on Plasma Phys. and Contr. Fusion*, Montreux, 17-21 June, 2002, ECA Vol, 26B P-2.026 (2002)
- [12] R. S. Sigmond, "Simple approximate treatment of unipolar space-charge-dominated coronas: The Warburg law and the saturation current", *J. Appl. Phys.*, 53(2), 1982, pp. 891-898

- [13] B. L. Henson, "A derivation of Warburg's law for point to plane coronas", *J. Appl. Phys.*, 52(6), 1981, pp. 3921-3923
- [14] B. L. Henson, "Derivation of the current-potential equation for steady point-to-plane corona discharges", *J. Appl. Phys.*, 53(4), 1982, pp. 3305-3307
- [15] G. W. Dahlmann, et al, "High Q Achieved in Microwave Inductors Fabricated by Parallel Self-Assembly", *Proceedings of 11th International Conference on Solid-State Sensors and Actuators*, Germany, June-10-14, 2001
- [16] L. B. Loeb, *Fundamental Processes of Electrical Discharges in Gases*, John Wiley & Sons, 1939

Chapter 3: Charging And Collection Of Airborne Nanoparticles Using Microfabricated Corona Ionizer

Principles of Operation

The charging of the particles takes place within the drift region. As the airborne particles pass through the drift region, these low-energy electrons will attach themselves to the neutral particles upon contact. These electrons are driven towards the particles by both diffusion and by the virtue of the electric field between the discharge tip (pin) and the collection grid (plane). The charge density per particle and the required residence time for acquiring saturation charge are determined by both diffusion and field charging. There are established mathematical models for both diffusion and field charging. For combined diffusion and field charging, there are currently several empirical and semi-empirical models [1]. Cochet's charging model is used here because it accommodates all particle sizes and provides a closed form analytical equation for the particle saturation charge as shown in Equation 3.1. Figure 3.1 shows the number of elementary charges carried by a particle at saturation charge versus particle size using Equation 3.1 [1].

$$Q_p^\infty = \left\{ \left(1 + \frac{2\lambda}{d_p} \right)^2 + \left(\frac{2}{1 + \frac{2\lambda}{d_p}} \right) \left(\frac{\epsilon_r - 1}{\epsilon_r + 2} \right) \right\} \pi \epsilon_0 d_p^2 E \quad (3.1)$$

where Q_p^∞ is the particle saturation charge, λ is the mean free path of air at 298K, d_p is the diameter of the particle, ϵ_r is the electrical permittivity of the particle, ϵ_0 is the electrical permittivity of free space and E is the applied electric field.

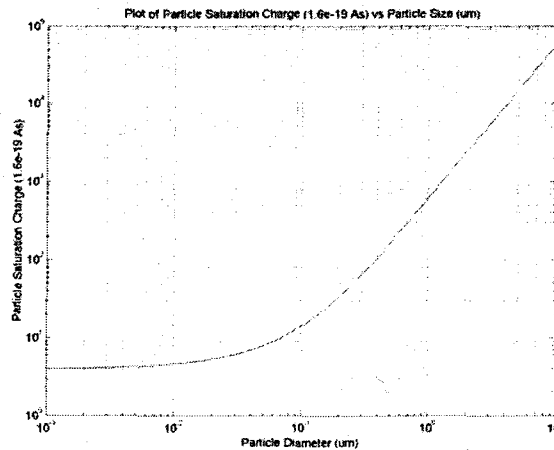


Figure 3.1: Analytical plot of number of elementary charge carried by a particle at saturation charge versus its size calculated at $\epsilon_r = 10$ (conservative) and $E = 2700V$ for a 2mm gap at a temperature of 298K.

The particle saturation charge is determined by both the particle properties and the operating parameters of the electrostatic precipitator. The time dependence [1] of the particle saturation charge is given by Equations 3.2a and 3.2b.

$$Q_p(t) = Q_p^\infty \frac{t}{t + \tau_Q} \quad (3.2a)$$

$$\tau_Q \approx \frac{4\epsilon_0}{\frac{j_{NE}}{E}} \quad (3.2b)$$

where j_{NE} is the average current density on the collection grid, t is the particle's residence time in the electrostatic precipitator's drift region and τ_Q is a time constant indicative of the time required to charge a particle to half of its saturation charge.

The corona current density distribution on the collection grid can be approximated using Warburg's cosine power law [2] as given by Equation 3.3.

$$j = j_0 \cos^m \theta \quad (3.3)$$

where j is the current density spatially dependent on its location on the collection grid, j_0 is the maximum current density measured, θ is the angle subtended from the pin axis indicating the spatial location on the collection grid and $m = 4.65$ for a negative discharge.

The corona current density approaches zero as the cone angle θ increases to 60° . The current limiting radius on the collection grid r_{limit} is given by Equation 3.4 [2].

$$r_{limit} = D \tan \theta \quad (3.4)$$

where D is the pin to plane separation gap.

Using Equation 3.4, the upper and lower bounds of the current limiting radius are calculated as 3.8mm and 3.1mm for pin to plane separation gaps of 2.2mm and 1.8mm respectively. It is reasonable to divide the operating corona current of $20\mu A$ by the collection grid area of $3.5mm^2$ (neglecting the grid effect) to obtain a conservative estimate for j_{NE} . Since the charging takes place in the drift region, the relevant electric field can be approximated as a uniform field between the precipitator electrodes. For an operating voltage of 2.7 kV, the maximum value of τ_Q is calculated to be in the order of few tens of microseconds. Therefore it can be assumed that most of the particles that are collected by the precipitator had obtained their respective saturation charge. Particle sizes approximately 250nm in diameter correspond to the lowest electrical mobility attainable. In a given electric field, these particles travel at the lowest electrical drift velocity. The electrical drift velocity of a particle V_{drift} is given by [3, 4].

$$V_{drift} = \frac{qC_c E}{3\pi\mu d_p} \quad (3.5)$$

where q is the particle charge, μ is the dynamic viscosity of air ($1.8e-5$ kg/m/s at 298K and 1 atm), E is the applied electric field, d_p is the particle diameter and C_c is the Cunningham slip correction factor given by Equation 3.6a [4] with its alternative form given by Equation 3.6b [5].

$$C_c = 1 + k_n \left[1.257 + 0.4 \exp\left(-\frac{1.1}{k_n}\right) \right] \quad (3.6a)$$

$$C_c = 1 + 1.647k_n \quad (3.6b)$$

$$k_n = \frac{2\lambda}{d_p}$$

where k_n is Knudsen number given by $k_n = \frac{2\lambda}{d_p}$, λ is the mean free path of air at 298K and d_p is particle diameter. Since the number of elementary charges per particle q for small particle size is almost the same, V_{drift} varies inversely with d_p .

The electrical drift velocity calculated for a 250nm particle under a uniform electric field given by 2.7 kV across a 1.8mm gap spacing is approximately 500mm/s. The maximum flow velocity of the aerosol used in the experiment is in the order of 40mm/s. Since both the gap spacing and the width of the collection grid is on the same order of magnitude, it can be assumed that the variation of flow velocities in the experiment does not have a significant effect on the precipitator's collection efficiency.

Experimental Setup and Results

The experimental setup consists of TSI 3076 constant output atomizer serving as aerosol generator and an environmental test chamber where the precipitator is mounted as shown in Figure 3.2. The aerosol generated is a suspension of liquid phase polydispersed oleic acid nanoparticles in ambient air. The particle size and number distribution of the aerosol output has been measured using TSI 3080/3081 Scanning Mobility Particulate Sizer. The particle size ranges from 30nm to 300nm and the particle geometric mean diameter is 70nm. The packaged microfabricated electrostatic precipitator is mounted on a jig.

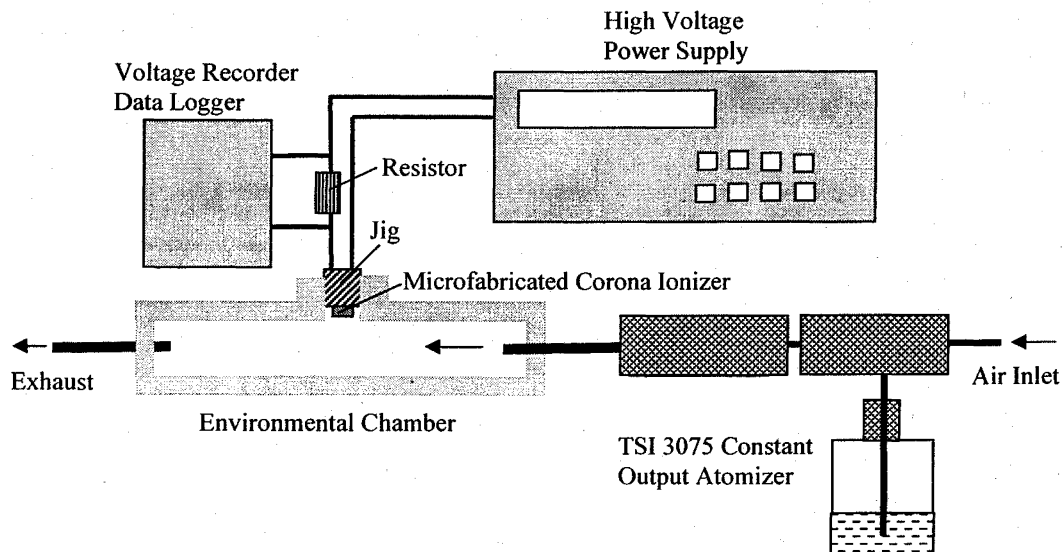


Figure 3.2: Schematic of experimental setup for precipitation of oleic acid nanoparticles.

It is positioned in the sidewall of the environmental chamber to minimize deposition via means other than electrical charging and precipitation.

The aerosol is passed through the environmental chamber at 1L/min via a needle valve. A diluting flow line is used to adjust the concentration of the nanoparticles within the environmental chamber via a separate needle valve. The aerosol is passed into an exhaust after exiting from the environmental chamber. The environmental chamber inlet flowrate is monitored using a flow meter. The operation of the precipitator is monitored via its corona current. The footprint of the precipitator is approximately 1cm^2 and it consumes approximately 200mW at $80\mu\text{A}$. The experiment is carried out under ambient conditions. The validation of successful collection of nanoparticles by the microfabricated electrostatic precipitator is carried by both visual observation and monitoring the resistivity change of the corona discharge "circuit". The resistivity monitoring is measured via a series resistor. The potential drop across the resistor is measured by a voltage recorder. Thus any change in the resistivity of the corona discharge "circuit" will result in a change in the corona current and is captured by the corresponding change in potential drop across the series resistor.

At the onset of the experiment, the precipitator is switched on and the corona current is adjusted to $80\mu\text{A}$. The needle valve is subsequently opened to allow the aerosol to pass into the environmental chamber. The corona current is observed to decrease after the aerosol is introduced, and recovers after the needle valve is closed. The experiment is carried out for precipitators with electrode gap spacing of 1.8mm and 2.0mm.

The corona current is observed to decrease after the introduction of the aerosol into the environmental chamber. This is due to the increase in resistivity due to accumulating oleic acid nanoparticles on the collection grid. Precipitated nanoparticles agglomerate and flow from the anode grid to its base (driven by minimization of Gibbs Free Energy and surface tension forces) as shown in Figure 3.3, allowing corona current recovery after aerosol exposure cutoff. This driving force is possibly a function of the volume of oleic acid residing on the grid. Figures 3.4 and 3.5 show the plot of corona current versus time elapsed for both precipitators. Both plots show varying corona currents that correspond to multiple aerosol exposure and cutoff. Forced dilution is also experimentally shown to accelerate corona current recovery as shown in Figure 3.6 (as indicated by the steeper recovery curve).

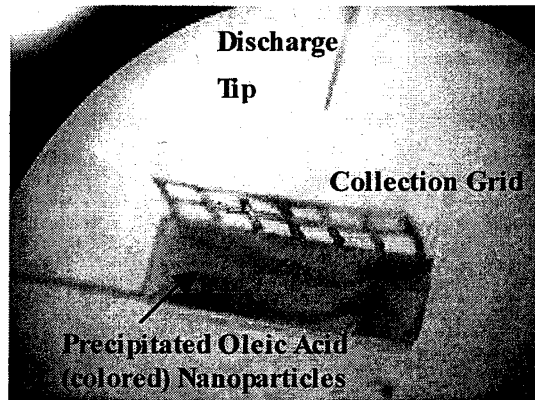


Figure 3.3: Photoprint of airborne oleic acid nanoparticles that were successfully charged and precipitated by the microfabricated electrostatic precipitator.

The dilution flow line is used to vary the concentration of the aerosol going into the environmental chamber to provide more discrete levels of nanoparticles concentration. The aerosol flow rate from the aerosol generator remains constant at 1L/min while the dilution flow varies from 0.12 L/min to 2 L/min to provide six discrete levels of nanoparticles concentration. Figure 3.7 shows the experimental plot of corona current versus the time elapsed as the nanoparticles concentration varies through the six discrete levels of concentrations for 2.2mm device.

Although the flow velocity in the environmental chamber changes with the nanoparticles concentration, it was shown earlier that it has no significant effect on the precipitator's collection efficiency. Therefore it is not necessary to adjust the aerosol flow rate to ensure that the flow velocity in the environmental chamber stays constant.

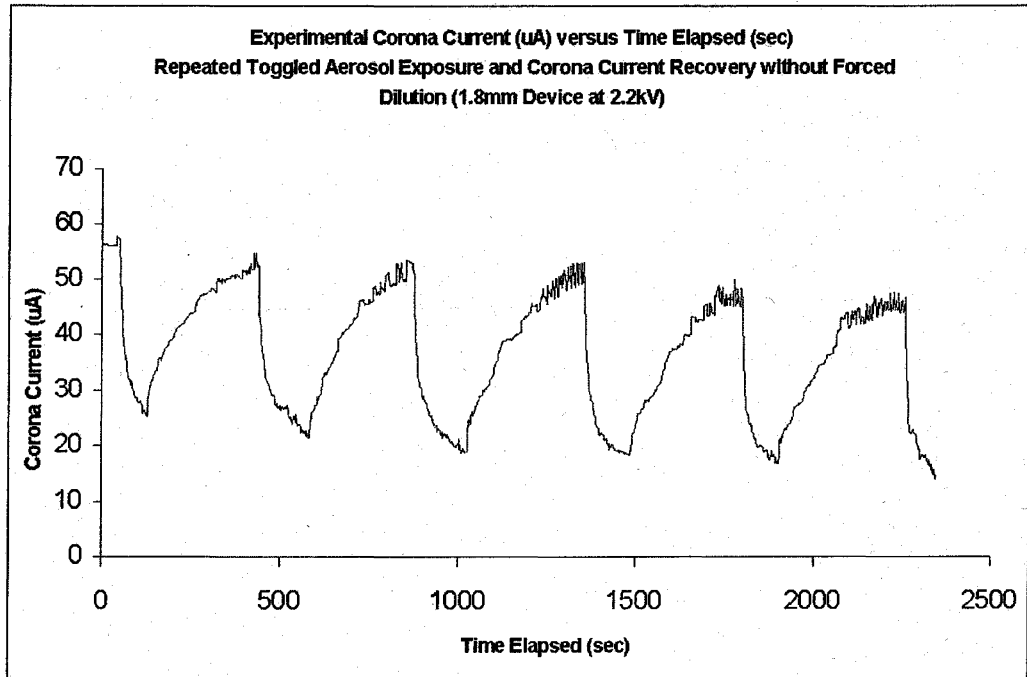


Figure 3.4: Plot of experimental corona current versus time elapsed for 1.8 mm device under repeated toggled aerosol exposure and recovery without forced dilution.

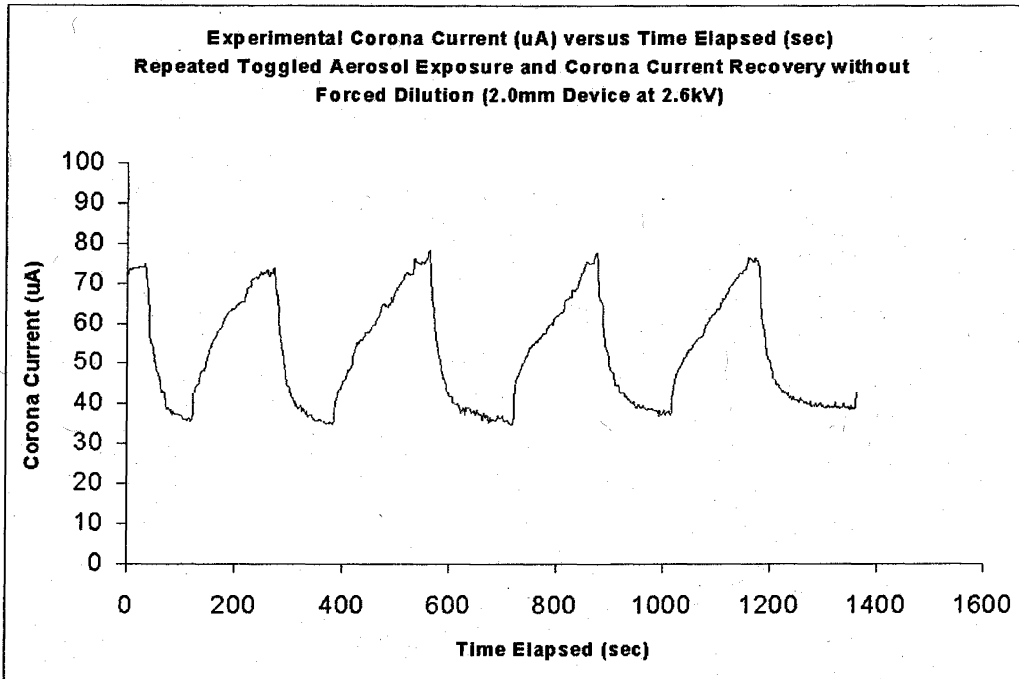


Figure 3.5: Plot of experimental corona current versus time elapsed for 2.0mm device under repeated toggled aerosol exposure and recovery without forced dilution.

Experimental Corona I-t Curve for Single Aerosol Exposure and Recovery with Forced Dilution (2.0mm Device)

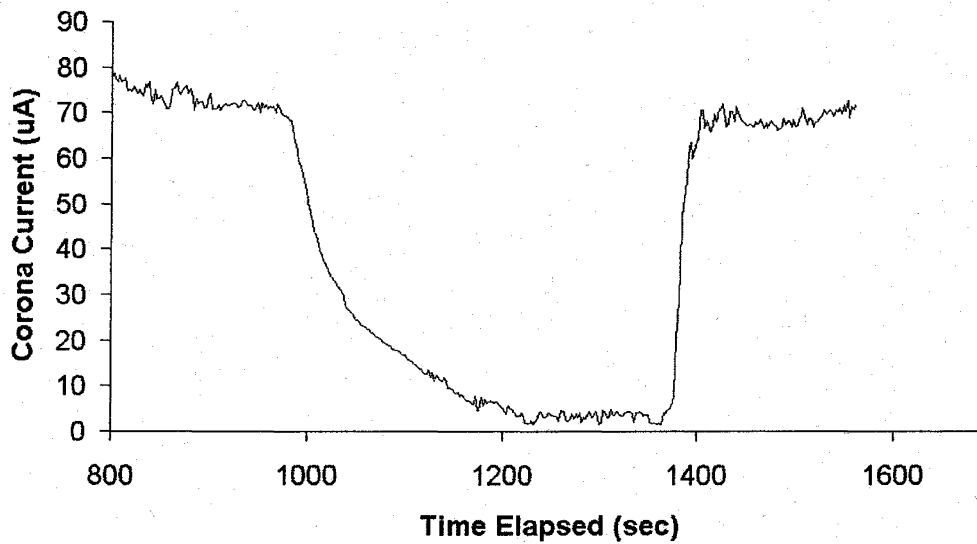


Figure 3.6: Experimental corona I-t plot of 2.0mm device under single aerosol exposure and forced dilution recovery. Forced dilution reduces concentration more rapidly, therefore accelerated the corona current recovery.

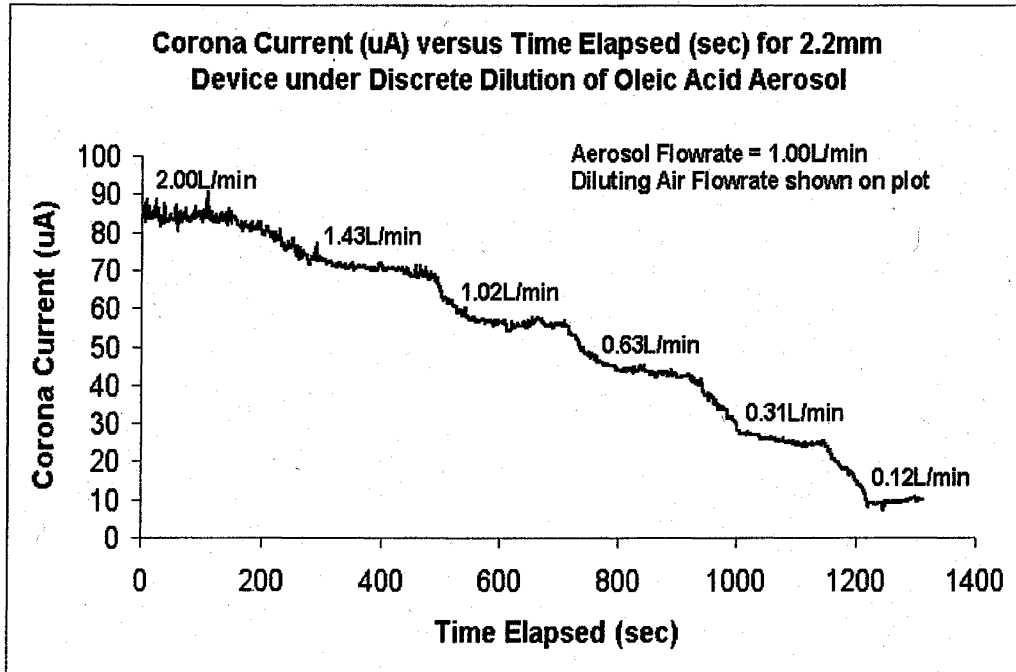


Figure 3.7: Experimental corona I-t plot of 2.2mm device for various oleic acid nanoparticles concentrations.

Analysis and Discussion

The nanoparticle flux to the collection grid of the precipitator for each concentration can be estimated given the corresponding resistivity changes and the nanoparticles number and size profile measured using the TSI Scanning Mobility Particulate Sizer (SMPS). To simplify the calculations, the oleic acid nanoparticles are assumed to precipitate uniformly on the collection grid and the rate of change of resistivity due to the precipitation is constant.

The rate of change of the precipitated nanoparticles layer thickness h on the collection

grid with respect to the corona current I_{corona} given as $\frac{dh}{dI_{corona}}$ can be calculated by relating the added resistance of the precipitated nanoparticles layer (hence its thickness) to the corresponding corona current. The rate of change of corona current I_{corona} with

respect to time t given as $\frac{dI_{corona}}{dt}$ can be derived from Figure 3.7 for each transition between concentration levels. Therefore the rate of change of the precipitated

nanoparticles layer thickness h with respect to time t given as $\frac{dh}{dt}$ can be made known as well. The number of nanoparticles can be calculated from their total volume using the number and size distribution profile. By relating the thickness h of the precipitated nanoparticles layer to its volume, the total number of nanoparticles arriving at the collection grid per unit time can thus be calculated. Table 3.1 shows the calculated total nanoparticles flux to the collection grid.

Table 3.1: Total nanoparticles flux to the collection grid.

Diluting L/min	Flowrate	Particle Concentration #/cm ³	Added Resistance MΩ	Approximate Nanoparticles Flux to Collection Grid #/sec	Total Flux to
1.43		1.23x10 ⁶	9	270	
1.02		1.49x10 ⁶	19	41 000	
0.63		1.84x10 ⁶	34	130 000	
0.31		2.29x10 ⁶	85	690 000	
0.12		2.68x10 ⁶	278	6 700 000	

To improve the accuracy of the calculated total nanoparticles flux to the collection grid, a configuration specific particle transport model will have to be developed. It will probably have to include a more accurate representation of the current limiting area using Warburg's law and the particles agglomeration effect. Significant further analytical and experimental work is required to establish the grade efficiency of the microfabricated electrostatic precipitator.

One major limitation of the microfabricated electrostatic precipitator in practical applications is the rapid build-up of collected particles on its collection grid. The build-up will possibly cause back-corona and deteriorates its performance. However it will be inexpensive to replace and dispose due to its low cost microfabrication process and non-toxic nature of the materials used.

Chapter References

- [1] K. R. Parker, *Applied Electrostatic Precipitation*, Blackie Academic & Professional, London, 1997
- [2] B. L. Henson, "A derivation of Warburg's law for point to plane coronas", *J. Appl. Phys.*, 52(6), 1981, pp. 3921-3923

- [3] W. C. Hinds, *Aerosol Technology: Properties, Behavior and Measurement of Airborne Particles*, John Wiley & Sons, 1999
- [4] J. H. Seinfeld and S. N. Pandis, *Atmospheric Chemistry and Physics: From Air Pollution to Climate Change*, John Wiley & Sons, 1998
- [5] A. S. Wexler and M. V. Johnson, *Real Time Single Particle Analysis*, Aerosol Measurement, edited by P. A. Baron and K. Wileke ; Ch 13, pp. 371, John Wiley & Sons, 2001

Additional Readings

- J. H. Seinfeld and S. N. Pandis, *Atmospheric Chemistry and Physics: From Air Pollution to Climate Change*, 2nd ed., John Wiley & Sons Inc, 1997
- B. L. Chua., et al, "A unipolar corona discharge microfabricated ionizer structure for gases at atmospheric pressure and composition", *17th IEEE International Conference on Micro Electro Mechanical Systems*, IEEE, Maastricht, The Netherlands, 2004, pp. 261-264
- A. Brauning-Demian, O. Hohn, T. Jahnke and C. Penache, "Micro structure electrodes: A new multipurpose plasma source", *GSI Scientific Report*, 2001, pp. 114-115
- G. Petzold, P. Siebert and J. Muller, "A micromachined electron beam ion source", *Sensors and Actuators, B*, **67** (2000), pp. 101-111
- R. Longwitz, H. van Lintel, R. Carr, C. Hollenstein and P. Renaud, "Study of gas ionization schemes for micro devices", *The 11th International Conference on Solid-State Sensors and Actuators (Transducers '01)*, Munich, Germany, June 10-14, 2001, pp. 1258-1261

Chapter 4: Separation Of Airborne Particles Using Microfabricated Corona Ionizer With Integrated Separator Electrodes (Mini-DMA)

Introduction

This chapter introduces a new pin-between-plane design for the microfabricated corona ionizer to reduce particle loss during the charging process as well as to facilitate packaging. The new design is integrated with a pair of separator electrodes on the same substrate. Airborne particle charging and electrostatic manipulation can be performed sequentially on the device. The main application of the device is for high performance (low pressure loss, high efficiency and flow rate) and localized air filtration systems.

Common air filtration methods [1] include inertia impaction, sedimentation and electrostatic precipitation. Inertia impaction based filters include HEPA filters and cyclone dust collectors. HEPA filters remove small particles at a significant air pressure loss. Cyclone dust collectors only remove large particles. Electrostatic precipitation collects both small and large particles, but has an issue of possible re-entrainment of particles back into the air stream. Sedimentation only works for large and heavy particles. All three methods required significant maintenance.

Among these methods, electrostatic precipitation has the widest particle collection size range varying from 1000 μ m to 10nm at a minimum pressure loss. The precipitation method has also been miniaturized and collection of airborne nanoparticles demonstrated [2, 3]. In an electrostatic precipitator, a corona discharge is set up between an asymmetrical electrode pair. The particles acquire electrical charges as they pass through the drift region of the corona discharge. Under the influence of the strong electric field between the electrodes, the particles migrate towards the plane electrode. The plane electrode serves as a particle collection plate. It is not uncommon for an electrostatic precipitator to have a collection efficiency of 99.9%. However particles build up rapidly on the collection plate, increasing the resistivity and eventually induce a back corona. The particles upon contact with the collection plate lose their electrical charge and might re-enter the airflow. In an electrostatic precipitator, the collected particles stay within the system. A micromachined air filter configuration that uses a pin-between-planes unipolar corona charging and electrostatic separation is equivalent to an electrostatic precipitator, in terms of particle collection efficiency and power consumption, without the need for a collection plate.

Principle of Operation

The filter configuration uses unipolar corona charging to charge the particles. The particles pass through the drift region of slow moving electron cloud. Corona charging is a combination of field charging and diffusion charging. There are several empirical and semi-empirical models that describe it [4]. Cochet's charging model is used to determine the particle saturation charge since it has an analytical solution for all particle sizes.

A pin-between-planes corona ionizer configuration, as shown in Figure 4.1, is used to improve the particle transmission efficiency. Ideally all the charged particles should leave the drift region of the corona discharge with the airflow. The proportion of particles trapped by the ionizer depends on the particles' residence time within the drift region, the applied voltage between the pin and planes, and the pin-to-plane gap distance. The residence time is a function of the aerosol flow rate and the tip distance from the edge of the parallel planes. A minimum overlap by the parallel planes over the pin is necessary for a stable discharge confined to the tip of the pin.

As shown in Figure 4.1, the particles first pass through the unipolar corona charger before entering the electrostatic separator. A voltage is applied between the separator electrodes to set up an electric field orthogonal to the airflow direction. The charged particles under the influence of the electric field migrate to one side of the airflow. The particles-laden flow and cleaned flow exit the system via separate outlet.

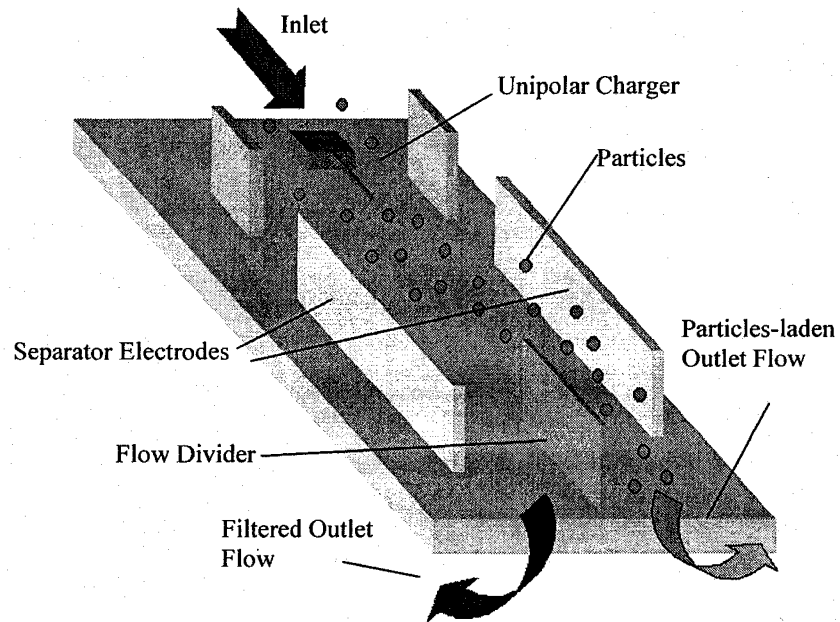


Figure 4.1: Schematic of the pin-between-planes corona ionizer with the separator electrodes showing the charging and manipulation of the airborne particles.

The separator electrodes' geometry allows sufficient residence time for the least electrically mobile particle to migrate effectively across to the particle-laden side when operating at reasonably high flow rate and a low applied voltage. This ensures all charged particles exiting the ionizer are removed from the cleaned flow. The volumetric ratio of cleaned and particle-laden flow rate is determined by the spatial placement of the flow divider. A corresponding higher separator electrodes' voltage is required for a higher cleaned-to-particle-laden volumetric flow rate ratio.

Since the particles have different electrical mobilities and initial spatial position, some of them will impact the separator electrode before they can exit. Upon impaction, the particles will lose their charge and are no longer influenced by the separator electrodes' electric field. They will not cross the streamlines over to the cleaned airflow. Diffusion is not a dominant particle transport phenomena within the separator due to the relative high flow velocity and short travel distance. The maximum flow rate is limited by the need to maintain laminar airflow, and low separator electrodes' voltage to prevent a sparkover. Pressure loss is minimized because there is no change in the channel size along its length and there is no obstructive structure in the channel. The efficiency of the filter configuration is limited by the charging efficiency of the unipolar corona ionizer. The residence time of the particles within the drift region of the discharge is significantly longer than the time required to charge the particles to near saturation. Table 4.1 shows a summary of the integrated corona ionizer and separator electrodes' key dimensions.

Table 4.1: Summary of device's key dimensions.

Channel Height	~1mm
Channel Width	~2mm
Separator Electrode Length	~1.5cm
Charger Discharge Tip Width	~20 μ m

The device is fabricated using the same low cost micromachining method based on large tolerance ($\pm 5\mu$ m) photolithography and low cost electroplating process [2] described in Chapter 2. Figure 4.2 shows the pre-package device.

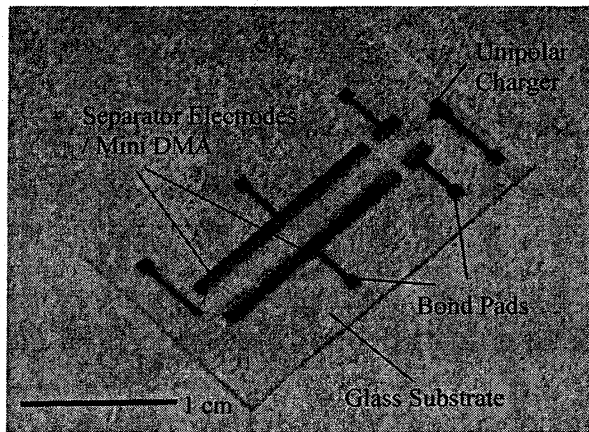


Figure 4.2: Photo print of pre-package device.

Experimental Setup and Results

The experimental setup consists of a packaged active filtration element, a pair of Faraday's cups, an air pump, a high voltage DC-DC converter and two Keithley 616 electrometers. Figure 4.3 shows the schematic of the experimental setup. Figure 4.4 shows the packaged device with two Faraday's cups.

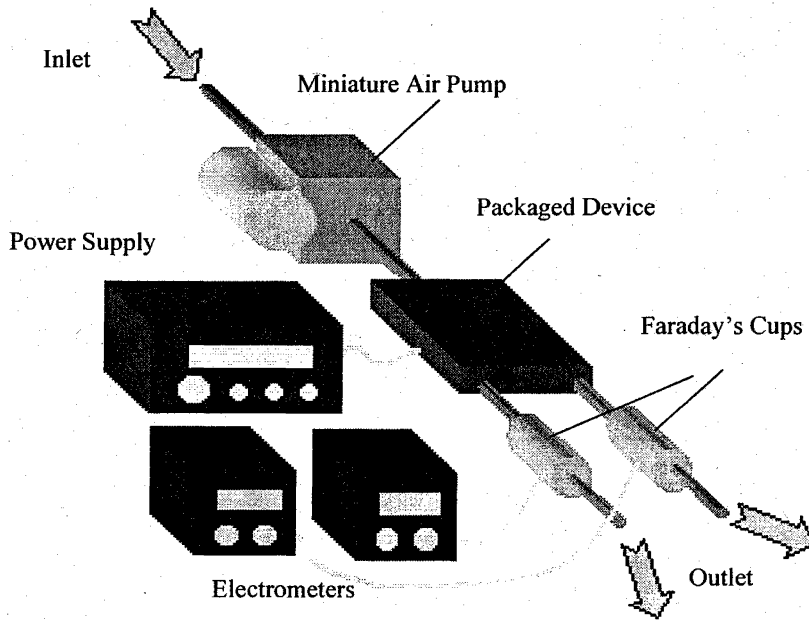


Figure 4.3: Schematic of experimental setup.

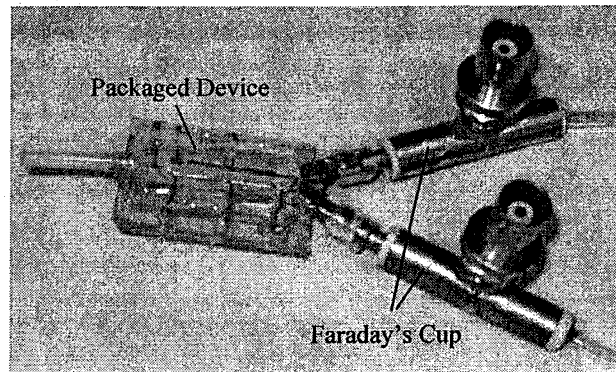


Figure 4.4: Photo print of packaged device with two Faraday's cups.

The device is manually packaged with an inlet and two outlets that correspond to the particle-laden and cleaned flows.

The device was tested in ambient air at RH $54 \pm 2\%$ and $22 \pm 2^\circ\text{C}$. A pair of Faraday's cups is used to monitor the charged particles from both particle-laden and cleaned outlets. Figure 4.5 shows the experimental relative Faraday's cup current and applied separator electrodes voltage plot for both outlets.

Particle-laden flow can be re-directed from one outlet to another by reversing separator electrodes' polarity. Figure 4.6 shows the Faraday's cup current of the particle-laden outlet as the separator electrode's voltage increases further. The decrease in the detected current is due to the increasing impaction of particles against the separator electrodes, thus losing their charge. The effect of various flow rates on the Faraday's cup current (particle-laden side) is shown in Figure 4.7. As the flow rate increases, fewer particles lose their charge through electrostatic impaction and therefore the detected current increases. Increasing from 1.25 L/min to 1.39 L/min (an 11% increase) doubles the current. This suggests that a huge fraction of the particles lose charge through electrostatic impaction with the separator electrodes.

The power consumption by the device is less than 4mW. The source of power consumption is the unipolar corona ionizer which is biased at approximately 1300V at $3\mu\text{A}$. Minimum power is consumed by the separator electrode pair, as there is no direct electrical current path between them.

With reference to Figure 4.5, the separation of charged particles is indicated by the respective increment and decrement of the Faraday's cup current for the respective outlet as the separation electrodes' voltage varies. The repeatability of the trend observed in the Faraday's cup currents in response to the change in separator electrodes' voltage is sufficient to demonstrate the proof of concept for the filtration element configuration.

For a more extended characterization of the filtration element configuration, laboratory generated aerosol with known composition with either liquid or solid phase particles

should be employed. Electrostatic precipitation of airborne pathogens has also been reported [4] and it is therefore probable to extend the application of the filtration element to removal of airborne pathogens.

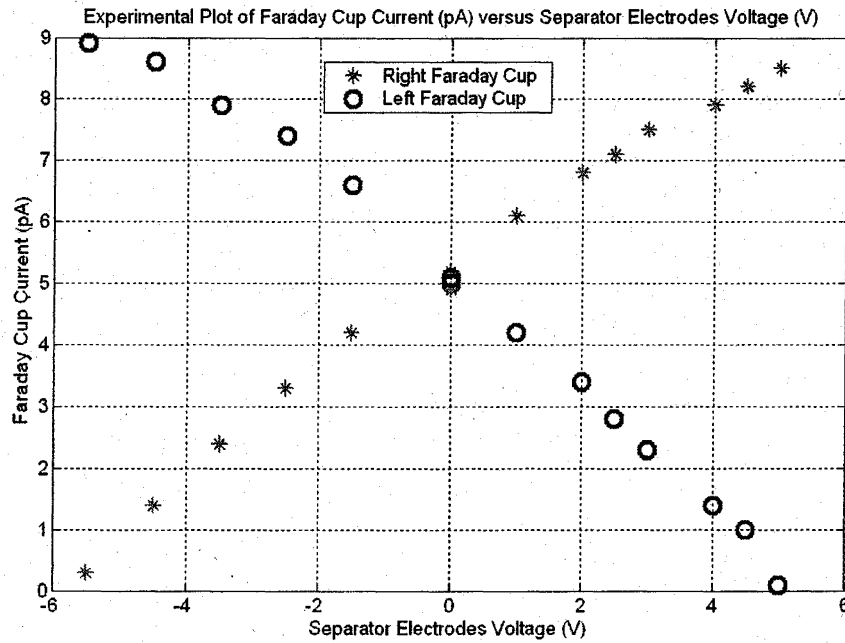


Figure 4.5: Experimental plot of Faraday's Cup's current (pA) versus separator electrodes' voltage (V).

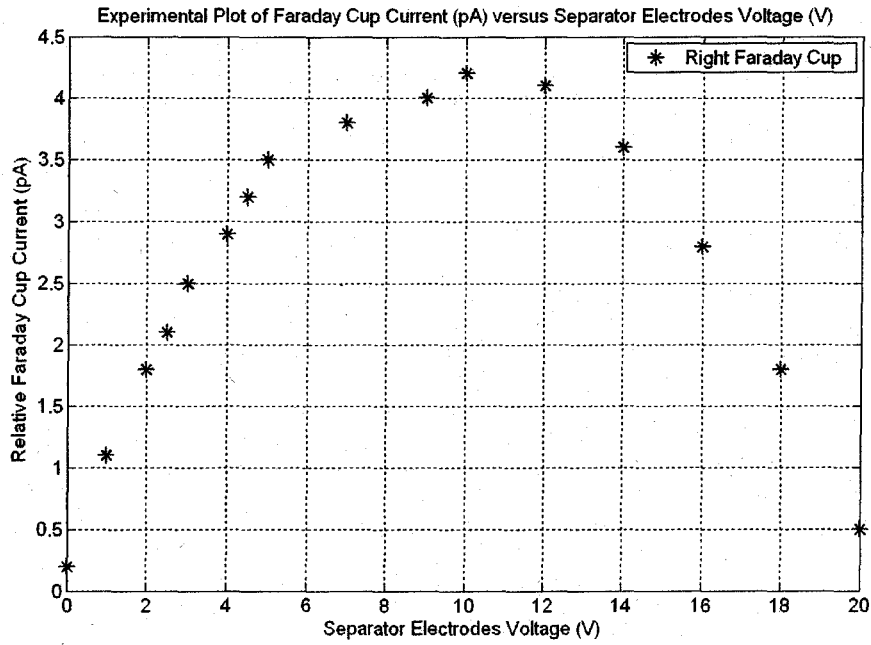


Figure 4.6: Experimental plot of detected current versus separator electrodes' voltage for Faraday's cup at particle-laden outlet.

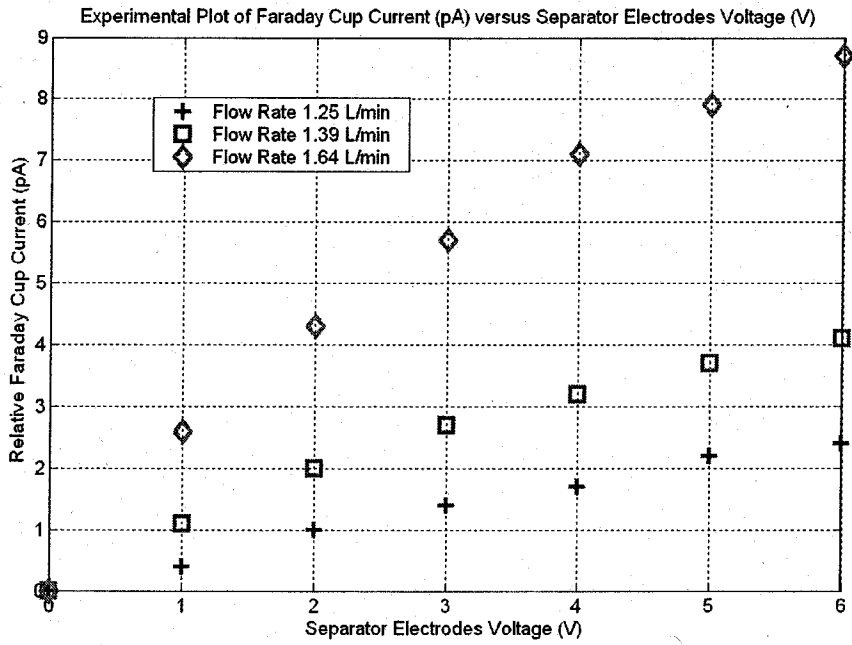


Figure 4.7: Experimental plot of detected current versus separator electrodes' voltage for Faraday's cup at particle-laden outlet for various flow rates.

References

- [1] K. R. Parker, *Applied Electrostatic Precipitation*, Blackie Academic & Professional, 1997
- [2] B. L. Chua, et al, "A unipolar corona discharge microfabricated ionizer structure for gases at atmospheric pressure and composition", in *Technical Proceedings 17th IEEE International Conference on Micro Electro Mechanical Systems*, Maastricht, The Netherlands, 2004, pp. 261-264
- [3] B. L. Chua, et al, "Collection of non-gas phase airborne nanoparticles by microfabricated electrostatic precipitator", in *Technical Proceedings CANEUS 2004 Conference on Micro-Nano-Technologies*, Monterey, 2004, AIAA 2004-6731, pp. 141-149
- [4] G. Mainelis, "Collection of airborne microorganisms by new electrostatic precipitator", *Journal of Electrostatics*, vol 33, 2002, pp 111-128

Chapter 5: Particle Sorting Using the Microfabricated Corona Ionizer And Separator Electrodes (Mini-DMA)

Device Level Principles of Operation

Sorting of airborne particles in accordance to their electrical mobilities is one of the fundamental principles used for aerosol measurement techniques. The electrical mobilities of particles can be unique to their geometrical diameters, depending on the method in which they are electrically charged. For diffusion and field charging, the electrical mobilities of the particles are unique to their geometrical diameters. For combined diffusion and field charging, particles with two geometrical diameters can share the same electrical mobility [1,2]. Passing the aerosol directly into the corona drift region results in combined charging. Alternatively, clean air can be passed over the corona drift region to carry the ions into a separate chamber where it is mixed with the aerosol. This results in diffusion-like charging with unique electrical mobility for each particle geometric size.

To demonstrate proof of concept in which the microfabricated corona ionizer and separator electrodes function as the particle charger and differential mobility analyzer (mini-DMA) respectively, we conducted a few experiments. At the time of project initiation, accurate particle sizing and counting instruments (able to detect several size bins below 100nm) were relatively large and costly. Smaller and less costly instruments were not able to distinguish several size bins if the particle size is less than 100nm. In the experiment, a range of nanoparticles with varying sizes is generated and passed through the microfabricated device. The corona ionizer performs the particle charging (referred to as the particle charger) and the separator electrodes carry out the sorting in accordance to the nanoparticles' electrical mobility (referred to as the mini-DMA). Figure 5.1 shows the two design variations of the pin-between-plane ionizer design experimentally investigated for the amount of particle loss during the charging process. The key difference in the two design variations is the distance of the tip of the pin from the edge of the grid as shown in Figure 5.1.

Experimental Setup and Procedure

Airborne oleic acid nanoparticles are generated using TSI 3076 Constant Output Atomizer. The nanoparticles generated are passed into TSI Scanning Mobility Particle Sizer that consists of TSI 3080 Electrostatic Classifier, TSI 3081 DMA and TSI3025A Condensation Particle Counter (CPC).

The microfabricated device is inserted into aerosol flow path between the DMA and the CPC as shown in Figure 5.2. The Electrostatic Classifier and DMA separate the oleic acid particles sequentially in accordance to their electrical mobilities. The stream passes through the particle charger/mini-DMA and into the CPC. When the microfabricated device is not in operation, the CPC registers and outputs the oleic acid particle size and concentration profile generated by the Constant Output Atomizer. This sets the reference baseline for the experiment.

In the particle charger, depending on the aerosol flow velocity, particles can be electrostatically trapped on the particle charger's grid due to the high electric field strength within the charging zone. To determine the amount of particle loss during the charging stage, the CPC measurement is first taken when the particle charger is inactive. This measurement is compared against that taken when the particle charger is active. The difference between the measurements gives the amount of particle loss during the charging stage as a function of their size. Particle Pass-through Ratio (PPR) is defined as the fraction of total particles that passes through the particle charger without getting trapped. An aerosol flow rate of 0.53 L/min is used within the particle charger. Note that each CPC measurement gives a full spectrum of particle

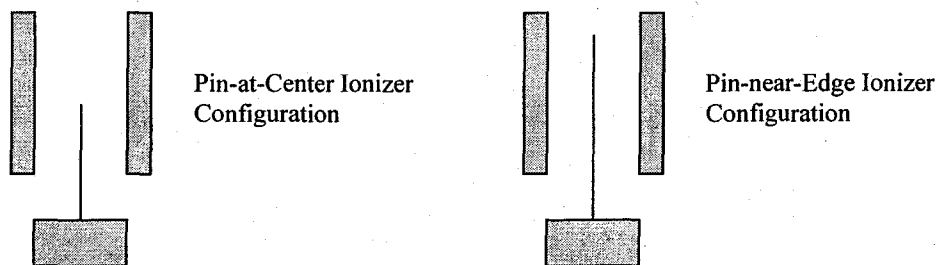


Figure 5.1: Two design variations of the particle charger used in the experiment.

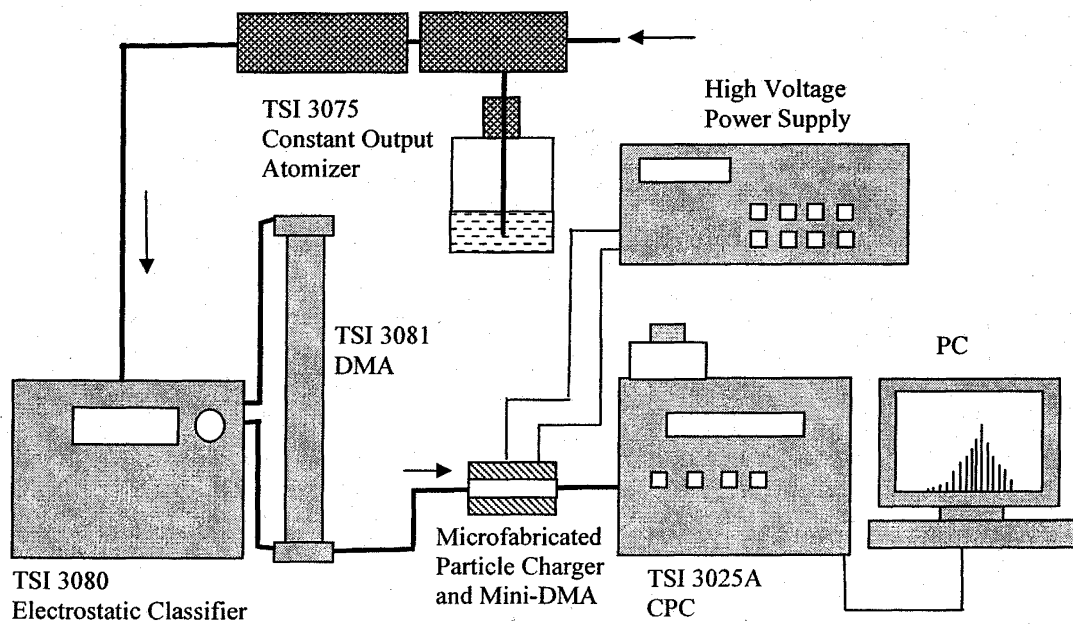


Figure 5.2: Schematic of experimental setup used for demonstrating the particle charger and mini-DMA.

size range from about 10nm to 300nm. Measurements are made for each value of particle charger operating voltage to investigate the respective PPR. The range of values for the particle charger operating voltage was from 0V to 2000V. The flow rate through the particle charger was about 0.53 LPM.

To demonstrate the particle sorting capability of the mini-DMA, a similar experiment was performed in which the operating voltage of the particle charger was kept constant. CPC measurements were taken for each mini-DMA voltage. The PPR will vary for various mini-DMA voltages.

Note that in direct corona charging (combined field and diffusion charging), the particle electrical mobility first decreases as the particle size becomes larger, and then increases when the particle becomes larger than 300nm [1]. In our experiment, the generated particle size cutoff was 300nm. Therefore, the particle electrical mobility corresponds to a unique particle size.

Particle Pass-Through-Ratio

Particle pass-through-ratio plots are shown in Figures 5.3 and 5.4 for various particle sizes and particle charger (ionizer) voltage. In both plots, the particle pass-through-ratio decreases after the inception of the particle charger. This is due to the electrostatic precipitation effect of the particle charger. As the particles acquire electrical charges as they pass through the charger, they are subjected to electrostatic forces exerted upon them by the charger's electric field. Consequently, some of the particles are lost as they drifted towards the charger's planes.

This experiment yields a few important results. First of all, it indicates a lower amount of particle loss for the pin-near-edge charger (ionizer) configuration as compared to pin-at-center configuration (Figure 5.1). This may be explained by the shorter particle residence time in the pin-near-edge configuration. The pin-near-edge configuration has a minimum particle pass-through-ratio of 80% while the pin-at-center configuration has a minimum particle pass-through-ratio of 65%. Overall both configurations are suitable for use as a particle charger.

The increase in particle pass-through-ratio as the charger's voltage increases (after an initial decrease) may be due to sputtering of the charger's electrodes or other plasma-chemical processes within the ionization zone. Continued investigation of this effect is warranted as part of future research.

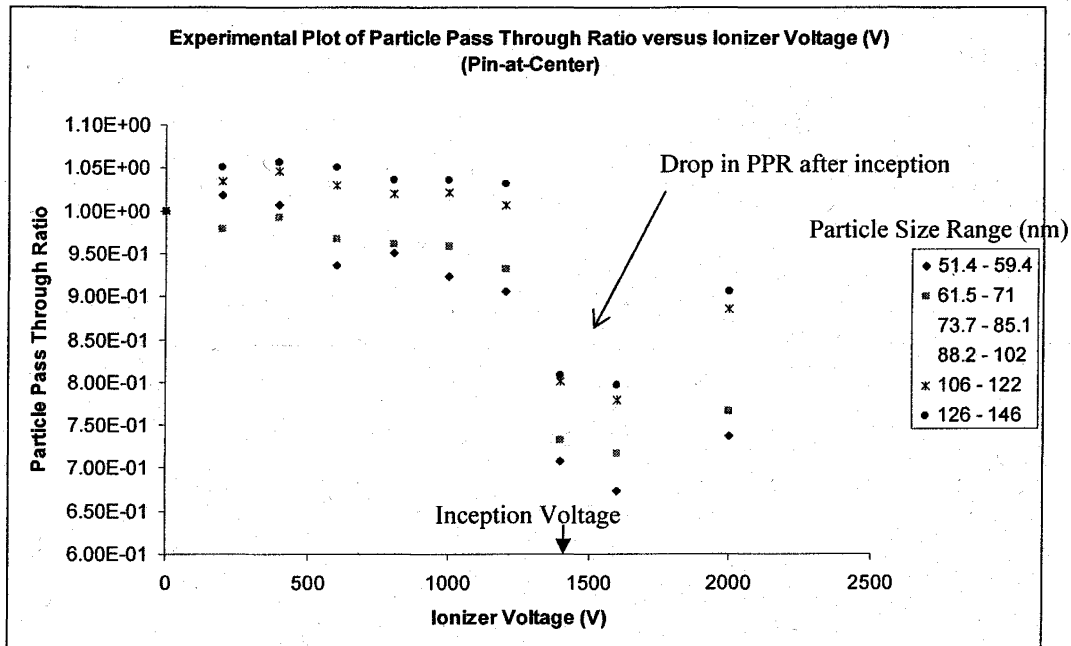


Figure 5.3: Experimental plot for particle pass-through-ratio versus ionizer voltage (V) for pin-in-center ionizer configuration and various particle size ranges. Flow rate is 0.5 LPM.

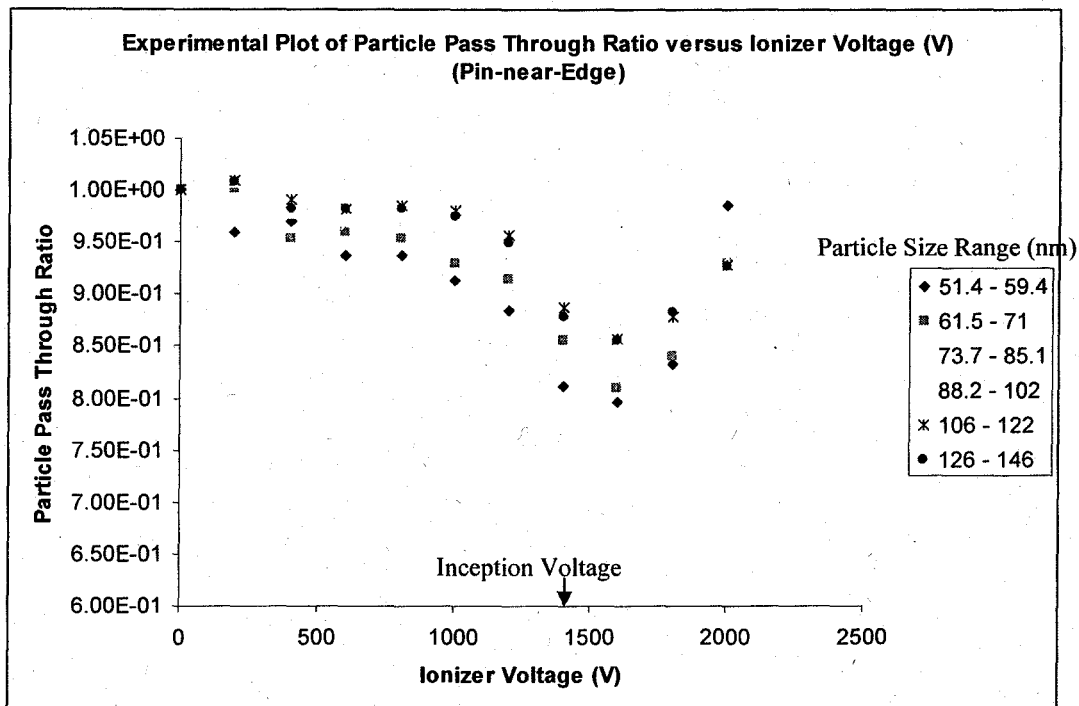


Figure 5.4: Experimental plot for particle pass-through-ratio versus ionizer voltage (V) for pin-near-edge ionizer configuration and various particle size ranges. Flow rate is 0.5 LPM.

Particle Sorting Results using the Mini-DMA

The primary objective of this experiment was to demonstrate a varying rate of change of particle pass-through-ratio versus the mini-DMA voltage (gradient of the plot) for various particle size ranges. As the mini-DMA voltage increases, the rate of change of particle pass-through-ratio for smaller particles was expected to be faster than that for larger particles. This is due to the higher electrical mobility for smaller particles as compared to larger particles (under the size of 300nm). For the same residence time within the mini-DMA, particles with higher electrical mobility travel further towards the mini-DMA electrodes.

For further elucidation, equation 5.1 shows basic relationship between particle drift velocity V , particle electrical mobility Z and electric field strength E between the mini-DMA electrodes.

$$V = ZE \quad (5.1)$$

It can be re-written as follows where $Dist$ is the distance traveled by the particle due to its electrical drift velocity and $t_{residence}$ is the residence time within the mini-DMA (Figure 5.5, pp 48):

$$\frac{Dist}{t_{residence}} = ZE \quad (5.2)$$

Using $Width$ as the width of the mini-DMA channel or the maximum distance which the particle can travel, Equation 5.2 can be re-written as:

$$\frac{Dist}{Width} = \frac{ZE}{t_{residence}} \quad (5.3)$$

$$\frac{Width - Dist}{Width} = \frac{Width}{Width} - \frac{ZE t_{residence}}{Width} \quad (5.4)$$

$$\frac{Width - Dist}{Width} = -Z \left(\frac{t_{residence}}{Width} \right) \left(\frac{1}{Width} \right) V_{applied} + \frac{Width}{Width} \quad (5.5)$$

where $V_{applied}$ is the applied voltage across the mini-DMA to generate the electric field strength E . Finally, Equation 5.5 can be re-written in terms of the particle pass-through-ratio PPR :

$$PPR = -Z \left(\frac{t_{residence}}{Width} \right) \left(\frac{1}{Width} \right) V_{applied} + 1 \quad (5.6)$$

From Equation 5.6, given a constant flow rate through the mini-DMA, the gradient from the plot of particle pass-through-ratio versus the mini-DMA voltage is directly proportional to the particle electrical mobility.

Figures 5.6 and 5.7 show the experimental plots of the particle pass-through-ratio versus the mini-DMA voltage for both pin-at-center and pin-near edge configurations. There are distinctive gradients for various particles sizes, indicating different electrical mobilities. The smallest particles having the highest electrical mobility also have the steepest gradient as anticipated by Equation 5.7. A steeper gradient indicates a higher particle velocity for a given electric field strength. At higher mini-DMA voltages, the difference in the electrical mobilities of the particles becomes more apparent. The pin-at-center configuration has a lower overall particle pass-through-ratio due to higher initial particle losses at the charger.

The mini-DMA voltage range ends at 2000V for pin-in-center configuration and 2200V for pin-near-edge configuration. This is due to the experimental limitation beyond which the mini-DMA begins to discharge. However this may be overcome by widening the electrode spacing in the mini-DMA.

These results confirm the ability of the microfabricated particle charger and mini-DMA to charge and separate airborne nanoparticles according to their electrical mobilities. This will enable the construction of a miniature and low cost airborne particle monitor that is capable of resolving particles smaller than 100nm.

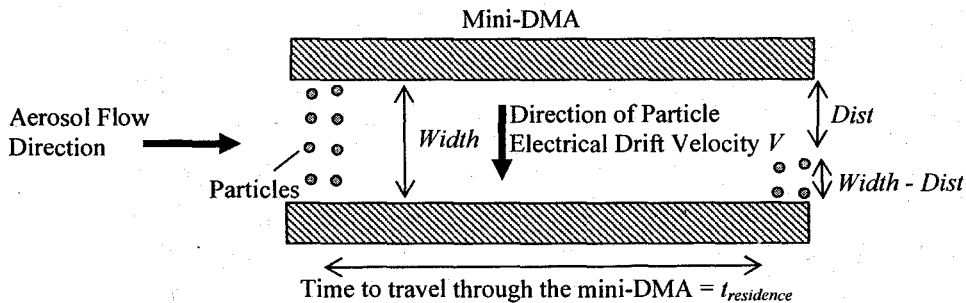


Figure 5.5: Schematic of mini-DMA and parameters used for computation of particle pass through ratio.

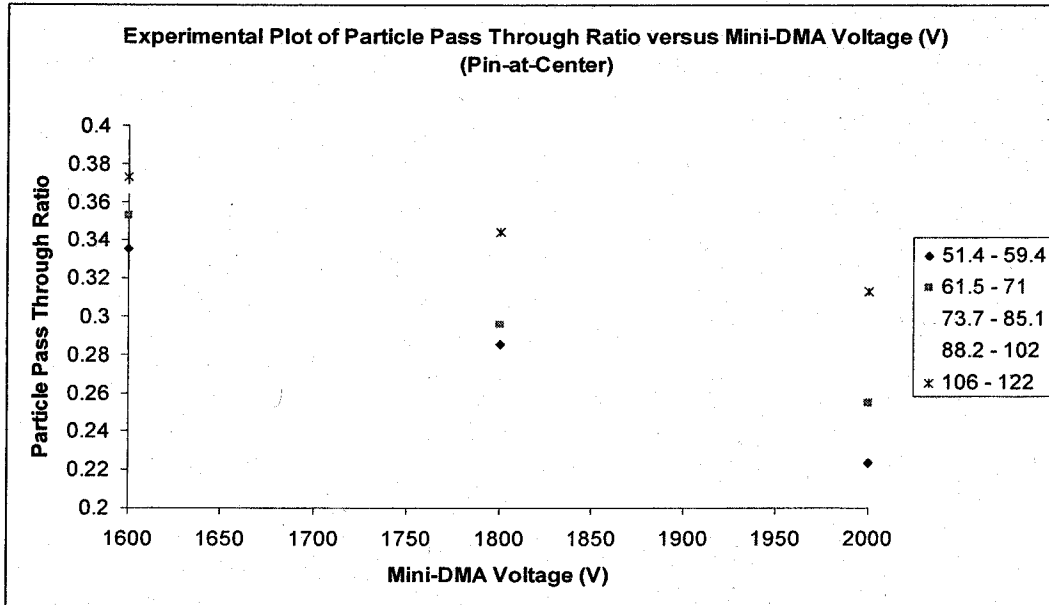


Figure 5.6: Experimental plot of particle pass-through-ratio versus mini-DMA voltage (V) for pin-at-center configuration.

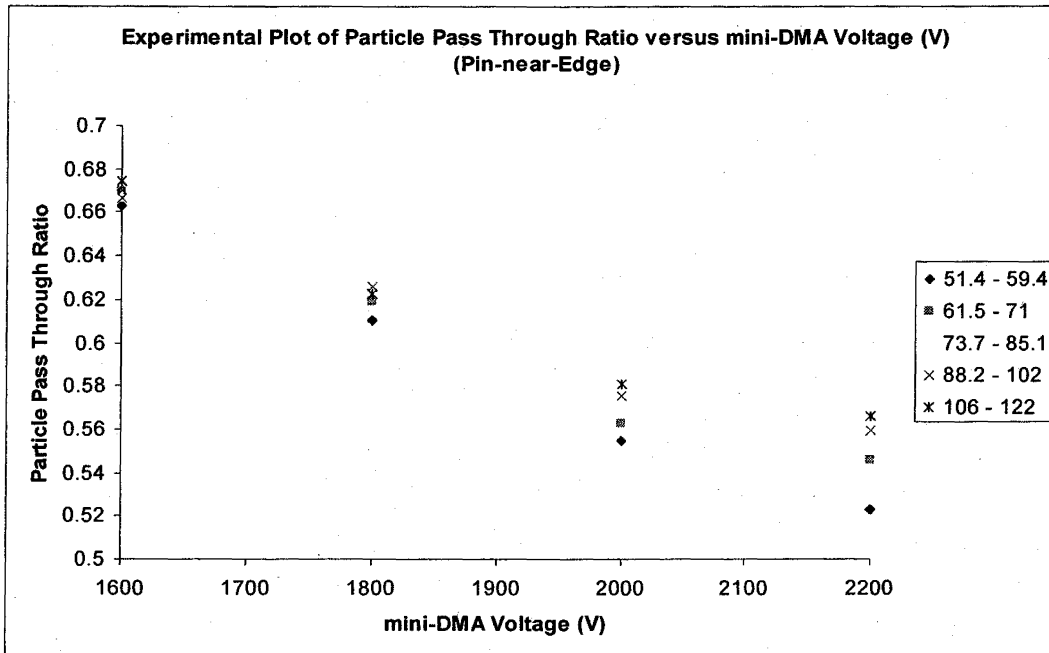


Figure 5.7: Experimental plot of particle pass through ratio versus mini-DMA voltage (V) for pin-near-edge configuration.

Experimental Electrical Mobility of Particles

The electrical mobilities of the particles were calculated from the experimental results. By assuming a uniform particle concentration, the particles' electrical mobilities can be obtained by re-arranging Equation 5.6 as follows:

$$Z = \frac{(1 - PPR)(Width)^2}{(t_{residence})(V_{applied})} \quad (5.7)$$

where values of PPR corresponding to specific values of $V_{applied}$ can be determined from Figures 5.6 and 5.7. $t_{residence}$ can be determined from the aerosol flow rate and the geometrical dimensions of the mini-DMA.

Figure 5.8 shows the experimental particle electrical mobility for various particle sizes. The trend of the plot is consistent with the understanding of combined charging where smaller particles have higher mobilities than larger particles (as long as they are smaller than 300nm). This plot also provides insight to the empirical charging model of the microfabricated particle charger.

Figure 5.9 shows the experimental particle electrical mobility plotted against the Cochet's analytical charging model. Both plots are of similar order of magnitude. The experimental data show that the electrical mobility is inversely proportional with diameter (for particles sizes < 300nm), as predicted by the model. The experimental electrical mobility differentiation is somewhat less than that anticipated by the analytical model. The discrepancy may be due to the higher number of elementary charges per particle for larger particle sizes as a result of the charging process. It may also be due to perturbation in the separator's electrodes' electric field due to charge accumulation. Higher differentiation is desired as it is translated into higher sensitivity or size resolution during measurement.

The differentiation of the experimental electrical mobility may be improved by reducing the flow rate and therefore increasing the particle's residence time within the mini-DMA. However, the reduction of flow rate will decrease the particle pass-through-ratio, resulting in fewer particles arriving at the mini-DMA. The other alternative to increase the particle's residence time with the mini-DMA is to increase the length of the mini-DMA. This will result in a larger device. Finally, the electrodes' spacing of the mini-DMA can be increased to accommodate higher electrical field strength before the onset of a partial discharge for larger electrical mobility differentiation.

The number of elementary charges per particle can also be deduced from the particle's size and its corresponding electrical mobility. In the actual measurement of ambient particle's size and concentration, the ambient aerosol is drawn into the microfabricated particle charger and mini-DMA. By measuring the change in detected current from particles exiting the mini-DMA, the particle flux and therefore concentration can be made known. The corresponding size distribution can then be deduced from the known particle electrical mobility.

Note that though the particles are charged by the Ni₆₃ bipolar charger in the TSI 3080 Electrostatic Classifier prior to entering the microfabricated particle charger, its effect has been observed experimentally to be insignificant.

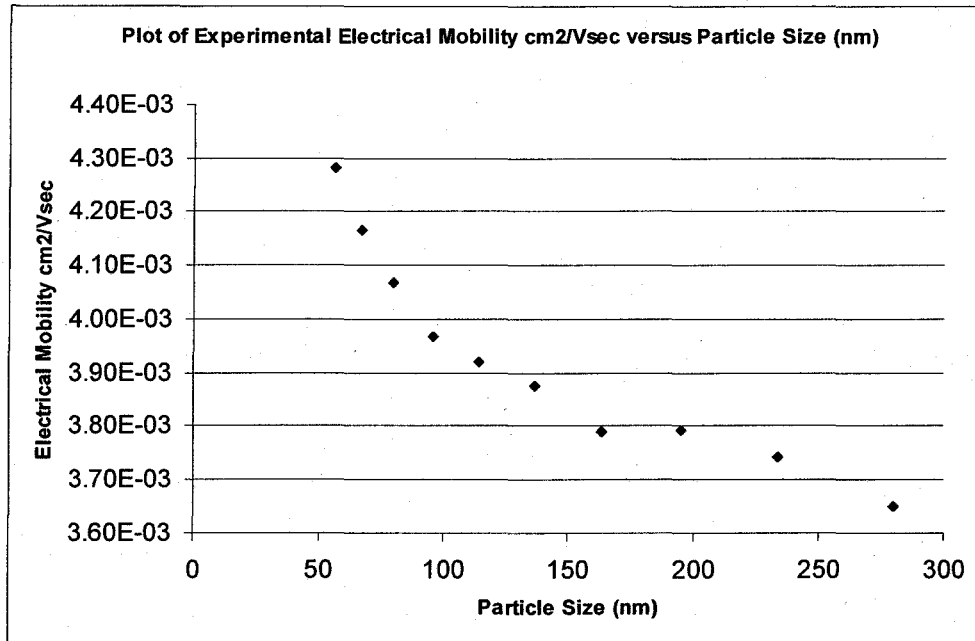


Figure 5.8: Experimental plot of particle electrical mobility (cm²/Vsec) versus the particle size (nm) derived from the test results using the microfabricated particle charger and mini-DMA.

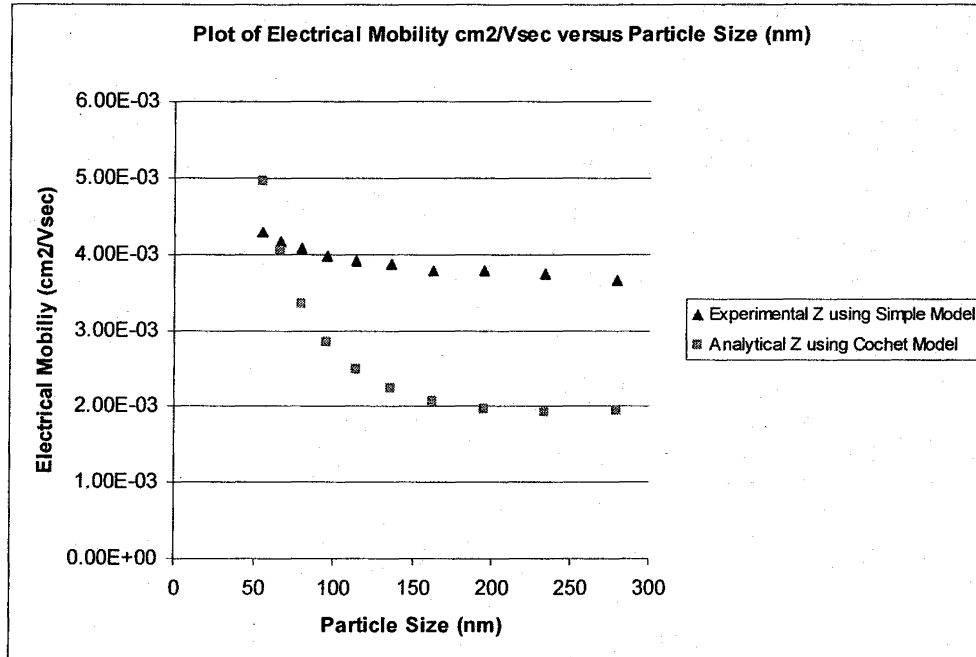


Figure 5.9: Experimentally obtained particle electrical mobility versus Cochet's analytical model.

Chapter References

- [1] W. C. Hinds, *Aerosol Technology: Properties, Behavior and Measurement of Airborne Particles*, John Wiley & Sons, 1999
- [2] K. R. Parker, *Applied Electrostatic Precipitation*, Blackie Academic & Professional, 1997

Chapter 6: System Level Integration and Operations

System Level Components

To create a fully functioning MicroAPA, we utilized a number of different commercial off the shelf components to complete the prototype. The additional components used at the system level integration consists of,

- Controller Board
- Miniature Air Pump and Flow meter
- High Voltage DC-DC Converter
- Faraday's Cup and Electrometer
- Wireless Serial Cable Replacement
- Batteries for Autonomous Power Supply

Each of these is discussed further below.

Controller Board

The function of a controller in the MicroAPA is to serve as an interface between the computer and all the components in the MicroAPA. It performs data acquisition, electrical power management, preliminary computation and sequential control. The controller provides power to the sensor and other peripheral components. It also reads the data coming in from the sensor and performs basic computation such as changing binary data into decimals. It also has an internal clock and allows timed pre-programmed sequence to be run independent of the computer.

The choice of controller board for the MicroAPA is the T100MD-888+ from Triangle Research International Inc. It provides multi-functional I/Os, 2 channels of A/D and 6 channels of D/A, PWM, Real-Time clock (MX-RTC), two serial ports and EEPROM Program/Data storage. It also has 8 digital I/Os. Two channels of A/D are assigned to vary the pump flow rate and the DMA voltage. Two channels of D/A are assigned to read the output from the electrometer and the flow meter. Digital channels are used to switch the power for the corona ionizer, flow meter and electrometer. Ladder logic and TBasic are used to program the controller. Figure 6.1 shows the GUI of the programming software.

The user control interface is shown in Figure 6.2 and it consists of inputs and relays which essentially function like buttons. By clicking and unclicking the buttons, the user can select either a manual or automatic mode for the MicroAPA.

In general, a small interface custom buffer circuit is required to connect the controller D/A output to the respective component such as the pump and the high voltage DC-DC. In the case of the pump, a high current op-amp (200mA, OPA 551) is used in the buffer circuit. They will provide the extra current required to power the pump.

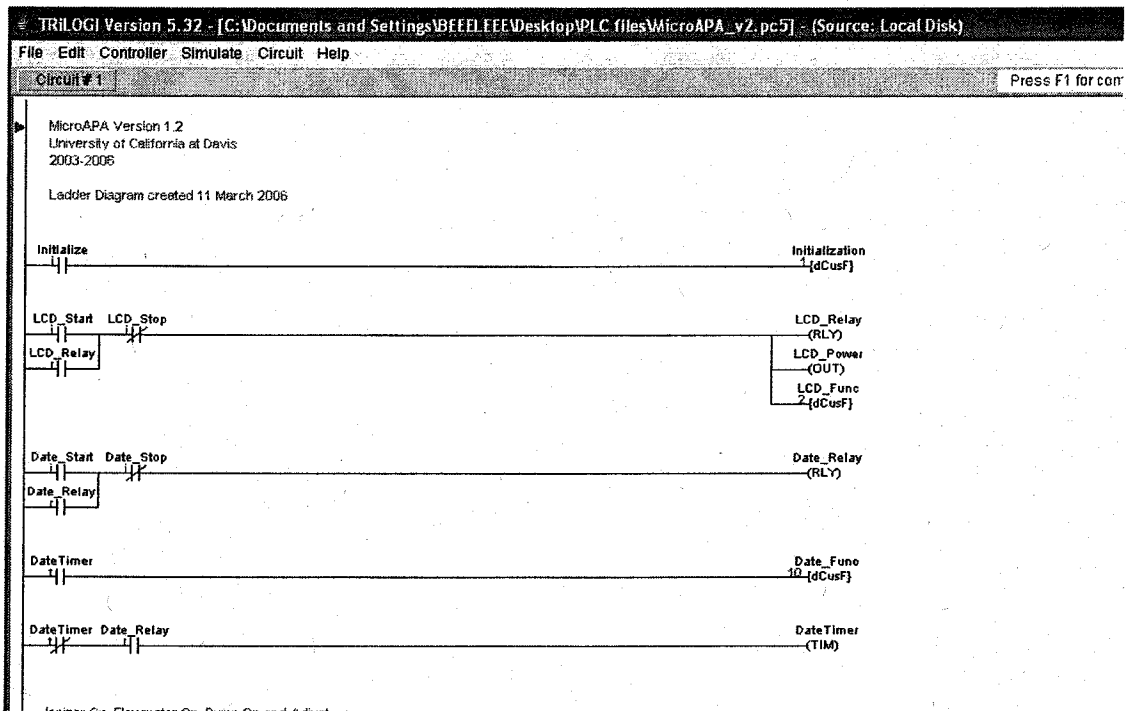


Figure 6.1: GUI of the Programming Software used for the Controller.

Programmable Logic Simulator

ADC1-8 View Select Control Pause Reset

Input	Timer	Counter	Relay	Output
Initialize	DateTimer		LCD_Relay	LCD_Power
LCD_Start	R_Stable		Date_Relay	EM_Power
LCD_Stop	Timer_100m		Emeter_R	Ionizer
Date_Start	TimerDMA		Ion_Relay	Flowmeter
Date_Stop	Timer_2sec		FlowM_r	
Manual	End_pump		PumpUp_R	
Emeter_ON	End_DMA		PumpDown_R	
Emeter_OFF			DMAup_R	
Ion_ON			DMAdown_R	
Ion_OFF			AutoRelay	
FlowMr_ON			Measure_R	
FlowMr_OFF			PumpAdjust	
PumpUp			Sweep_R	
PumpDown			DMAadjust	
DMAup			End_Relay	
DMAdown			Reset_R	
Measure				

Figure 6.2: User interface with the MicroAPA.

Pump and Flow Meter

The air pump used for the MicroAPA is the SENSIDYNE AAA series pump. The flow meter used for the monitoring the air pump is OMRON MEMS-based D6F Flow Sensor. The air pump takes in a voltage ranging from 0V- 10V and gives out up to 2 LPM. The operating flow rate of the MicroAPA is from 1-1.5 LPM.

High Voltage DC-DC Converter

The high voltage DC-DC converter used for the MicroAPA is from PICOELECTRONICS. The converter used for the ionizer is an AV Series while that used for the DMA is a VV Series. The key difference between the series is the input impedance. The AV series has significantly lower input impedance than the VV series. The AV series cannot be connected to the controller's D/A without an elaborate circuit. However, it can be connected the controller digital port without much problem.

Faraday's Cup and Electrometer

The Faraday's cup used in the MicroAPA consists of an inner cup and an outer shield as shown in Figure 6.3. The purpose of the bend in the air flow is to ensure no stray electric field from the high voltage DC-DC converter is registered by the inner cup. The capture mechanism of the Faraday's cup is by both diffusion and impaction. The small particles are captured by diffusion while the large particles are captured by impaction. The current mesh used is a nominal 2um stainless steel mesh.

The electrometer used is a custom designed electrometer by CERMAT Inc specifically for the MicroAPA project. It has a very narrow bandwidth and has a gain of 1V/pA. The full scale reading is 6V (for 6pA) and the baseline value is about 250V. It is sealed in a metal enclosure with its own 9V battery.

Wireless

GRIDCONNECT Bluetooth modules are selected to function as serial cable replacement. Currently the MicroAPA is connected to the computer via a serial cable. This serial cable can be replaced by either the GRIDCONNECT Bluetooth modules or any other wireless serial cable replacements that is widely available commercially.

Autonomous Power Supply

The MicroAPA currently uses NiCd rechargeable batteries. It allows the MicroAPA to function autonomously to allow sampling to be carried out. By having a better power management such as programming in SNOOZE mode, the battery life can be extended.

Potential Extended Capability

Digital thermometer and hygrometer capability can be added to the MicroAPA fairly easily. An off-the-shelf digital thermometer and hygrometer may have their analog output connected to the controller board A/D ports. The readings can then be accessed directly by the MicroAPA computer as part of the data output.

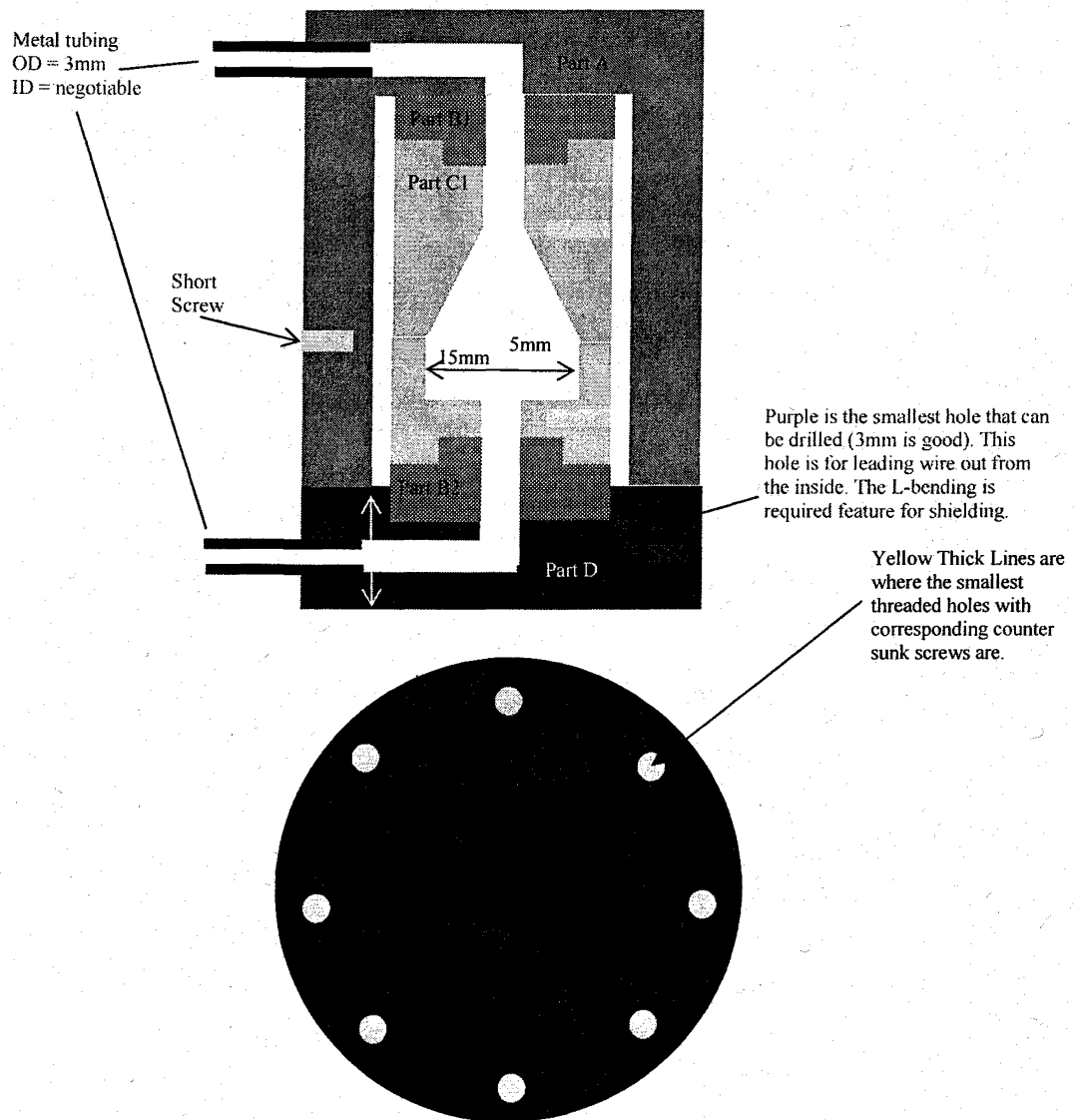


Figure 6.3: Drawings for the custom Faraday's Cup.

Integrated MicroAPA

Figures 6.4 and 6.5 shows the side view of Integrated MicroAPA with Faraday's cup, electrometer, LCD and power distribution cable. The Faraday's cup is connected to the electrometer via a BNC cable.

Figure 6.6 shows the top view of the MicroAPA and Figure 6.7 shows the MicroAPA with the computer. With reference to Figure 6.6, the corona ionizer and DMA is packaged in a shielded enclosure together with the high voltage DC-DC converter. This is to ensure that stray electric field from the high voltage DC-DC converter does not interrupt with the rest of the system. The relay switch is used to control the power supply to the buffer circuit. A separate power supply (another battery pack) is used to power the buffer circuit. The relay switch allows I/Os of the controller board to handle large electrical currents.

Figure 6.8 shows the MicroAPA and computer over I-80 freeway in Davis, CA. Figure 6.9 shows the MicroAPA packed in a carrier case and ready to go. Current battery packs permits about 10 scans before recharge is needed. Each scan takes about 2 minutes. The lifetime of the battery can be prolong by using a longer lifetime battery ($> 3000\text{mAH}$) and designing more power efficient circuitry. This is not an issue if the MicroAPA can be plug into an existing power line or supported by a significant larger battery (car battery). Note that even with a car battery, the SMPS would not be able to function.

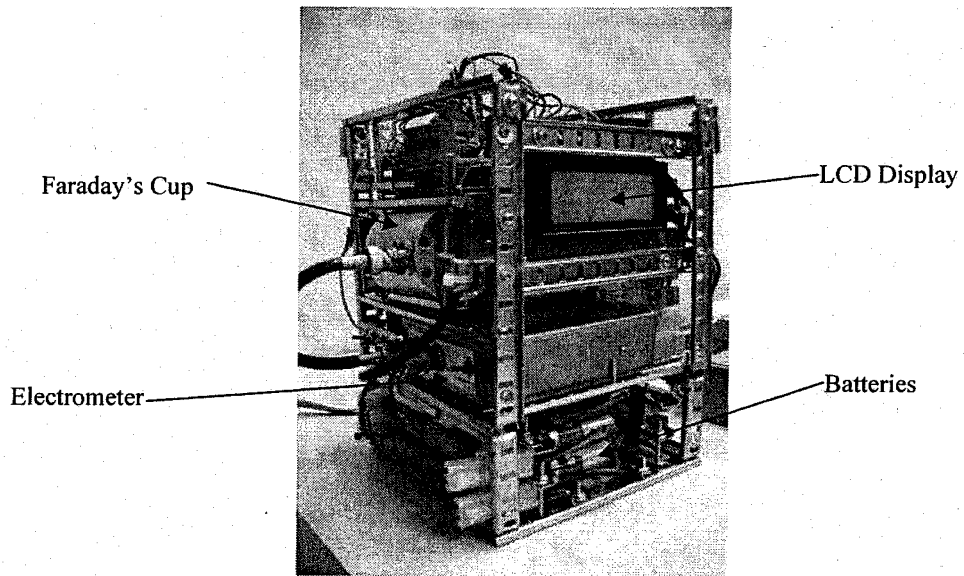


Figure 6.4: Integrated MicroAPA showing readings and settings in its LCD display.

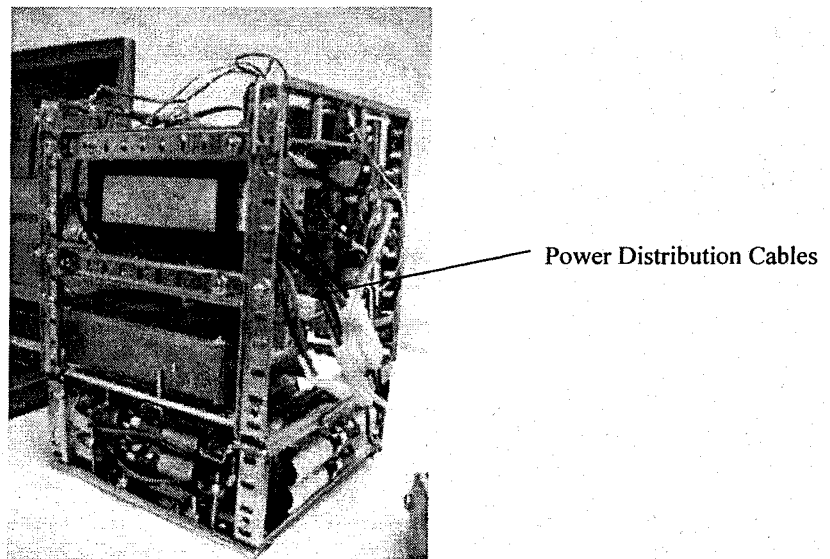


Figure 6.5: Integrated MicroAPA showing the power distribution cables.

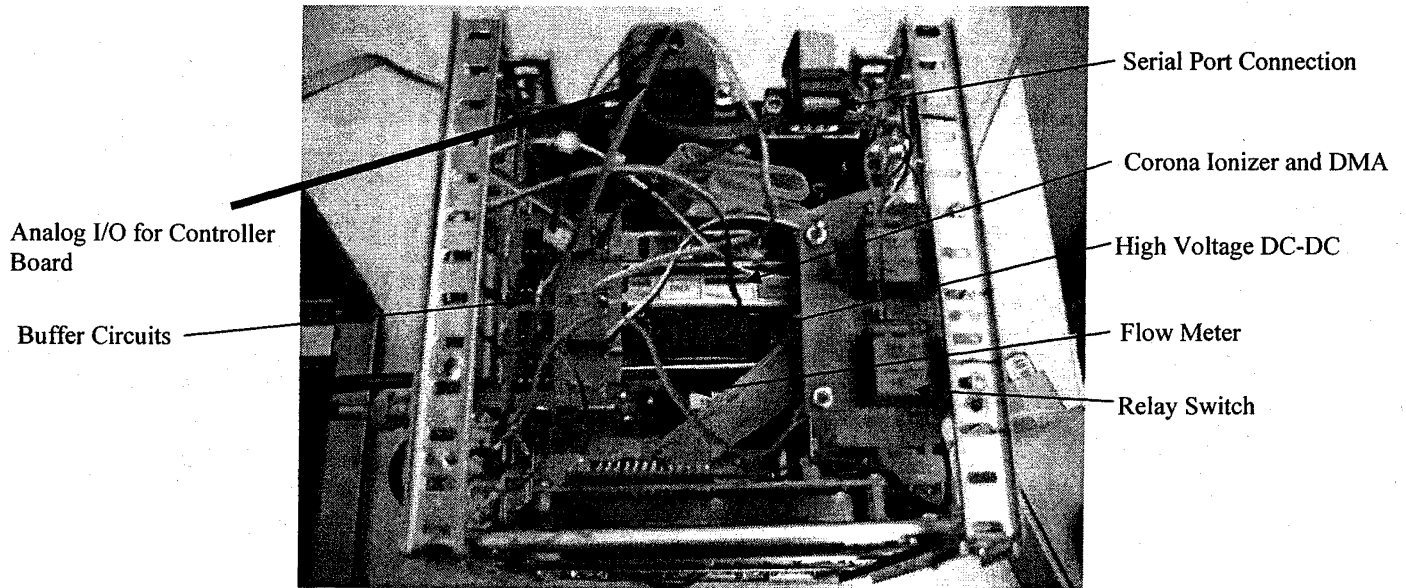


Figure 6.6: Top view of MicroAPA.

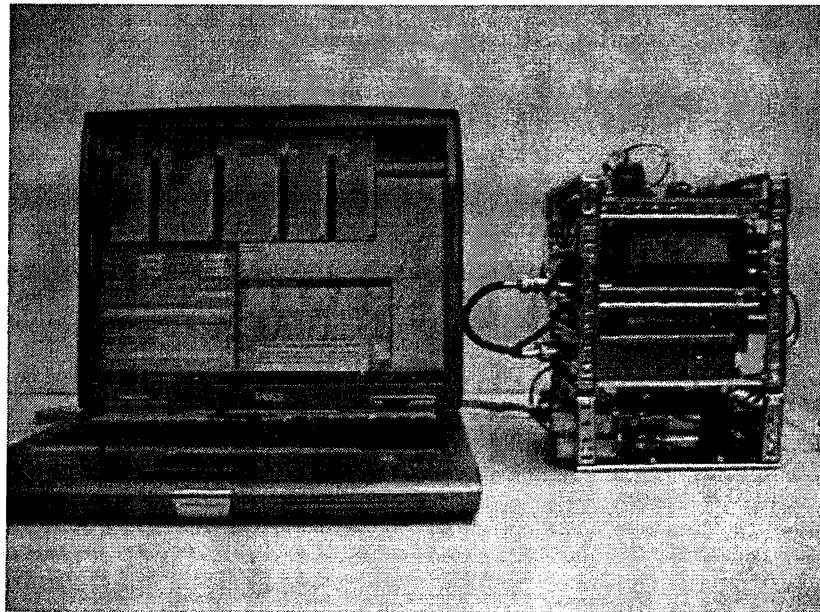


Figure 6.7: Computer with User Interface shown and MicroAPA.

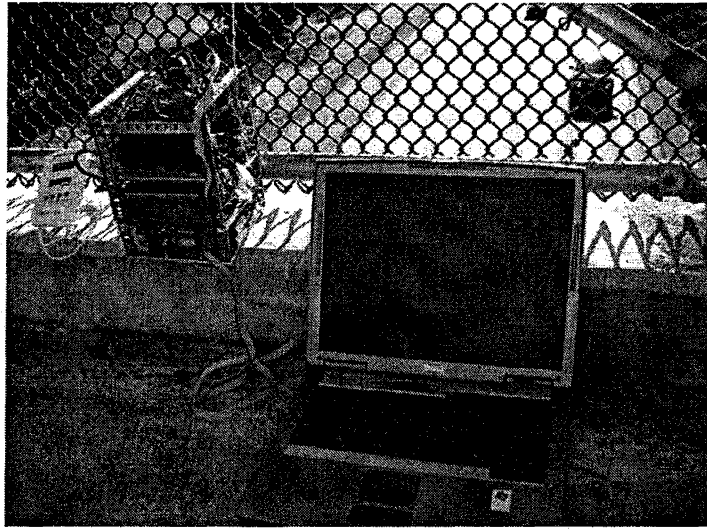


Figure 6.8: Demonstration of MicroAPA portability by deployment over I-80 Freeway in Davis, CA



Figure 6.9: MicroAPA packed and ready to go to the next measurement site.

Figure 6.10 shows the preliminary results from the integrated MicroAPA using the TSI 8075 Constant Output Atomizer as the aerosol source. The concentration of the aerosol is about 10^6 particles/cm³. The plot shows that as the Mini-DMA voltages increases, the current detected by the Faraday's current and hence, the output voltage of the electrometer decreases. This indicates that as the DMA voltage increases, it is pulling out particles with higher electrical mobilities, leaving those with lower electrical mobilities to arrive at the Faraday's cup to be counted. The maximum input voltage to the Mini-DMA is 110V maximum at the DMA's electrodes. The sample flow rate is 1.5LPM.

Figure 6.11 shows the raw data gathered from the field measurement shown in Figure 6.8. The trend from the result is not conclusive. As the DMA voltage increases, the electrometer current should decrease. Upon further investigation and comparison with the laboratory data, we believe there are several possible explanations:

- Data from Figure 6.8 was gathered from the laboratory using a 100V HV DC-DC converter (Picoelectronics Inc 5AV100). Fine voltage adjustment allows several voltage bins (less than 100V) to be applied across the mini-DMA's electrodes. The input tuning voltage for the HV DC-DC converter is derived from a regulated power supply. However, upon implementation for autonomous operation, the 100V HV DC-DC had to be replaced with a Picoelectronics Inc 5kV HV DC-DC due to impedance mismatch with the controller board DAC port. Since fine mini-DMA voltage tuning was not achieved in the autonomous MicroAPA, the measurement was not performed over the same DMA voltage range shown in Figure 6.10.
- The concentration in ambient air is at least one order of magnitude lower than that generated by the atomizer. To compensate for the lower concentration, measurement in ambient air has to be carried out at a higher flow rate. However, a higher flow rate will lower Faraday's cup residence time for smaller particles and therefore lower capture efficiency. This results in an overall lower electrometer current. The current flow rate is also limited by the size of the flow channel in the micro ionizer and mini-DMA. An excessive flow rate will result in turbulent flow within the mini-DMA.
- At programmed DMA voltages higher than 1000V, it requires an input voltage of 1V at the 5kV HV DC-DC converter. Due the large current consumed by the converter, the current circuitry was not able to keep a constant voltage at the DMA.

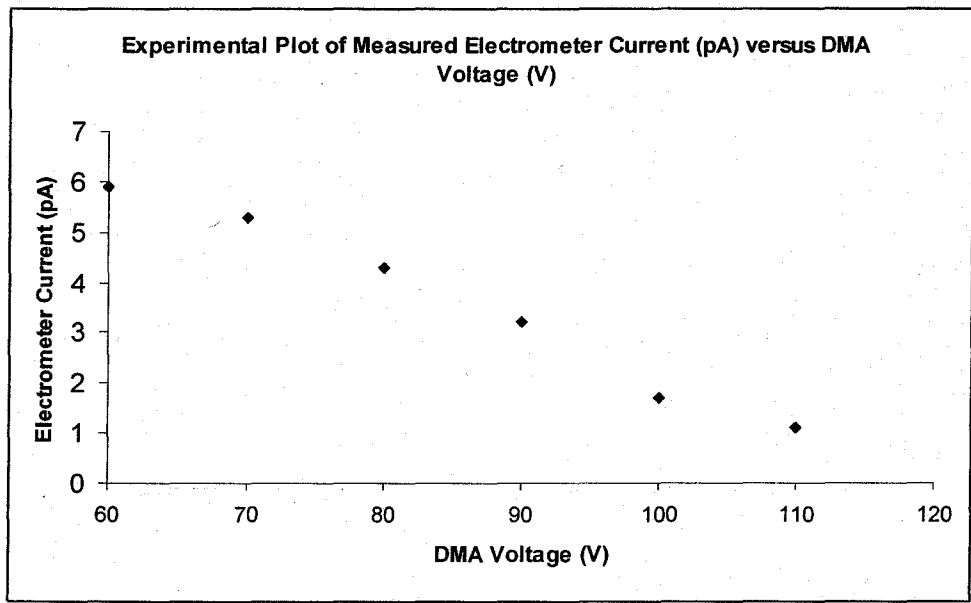


Figure 6.10: Experimental Plot of Measured MicroAPA Electrometer Current (pA) versus MicroAPA DMA voltage (V) using TSI 3075 Constant Output Atomizer as particle source at 1.5LPM sample flow rate.

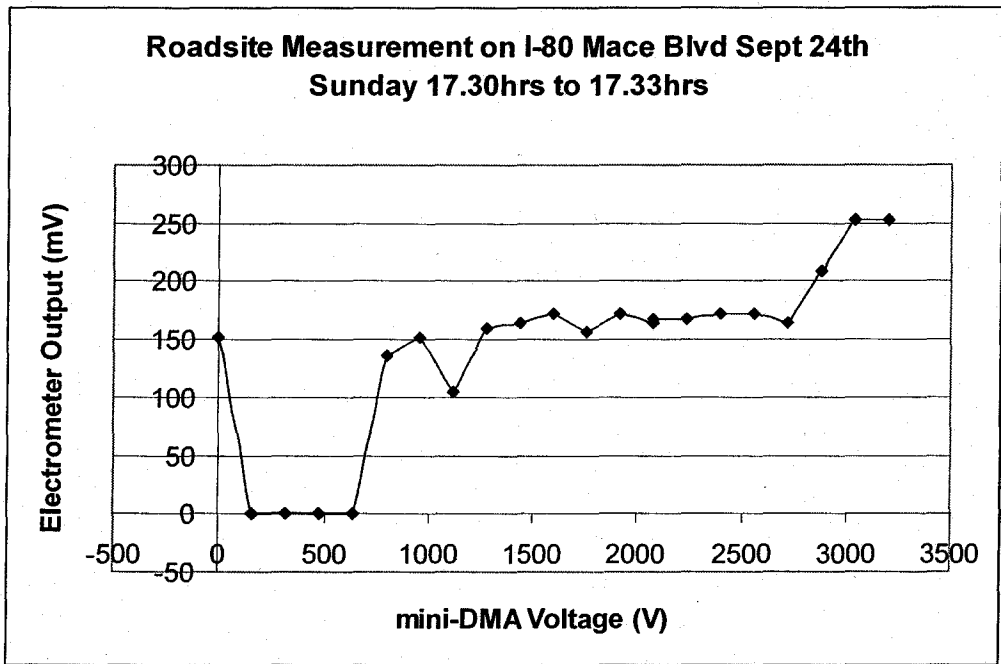


Figure 6.11: Experimental Plot of Measured MicroAPA Electrometer Current (pA) versus MicroAPA DMA voltage (V) at Roadsite Measurement on I-80 Mace Blvd Sept 24th Sunday

Conclusion

This work has clearly established the viability of the MicroAPA prototype. In addition, the ionizer breakthrough establishes the necessary foundation from which to extend the current design. Although a proof of concept for the MicroAPA has been performed, an autonomous unit of MicroAPA will require additional resources as well as expertise from other areas of engineering including analog circuit design and micro controller/processor programming. The first set of field experiments show that to go to scale, the MicroAPA may require,

- (a) First, a new controller board with very low output impedance for its DAC ports. The preliminary field tests output impedance of the current controller board is too high. This creates the need for buffer/amplifier/attenuation circuitry with even higher input impedance. As a result, some off-the-shelf components such as the Picoelectronics Inc 5AV100 cannot be used in the current version of the MicroAPA.
- (b) In place of a new controller board, a more elaborately designed buffer/amplifier/attenuation circuitry would be needed. This would require specialized analog circuit design which is beyond the scope of this project.
- (c) The detection sensitivity via signal processing, such as modulation of the electrical current from the Faraday's cup, should be increased. The current setup measures the DC signal from the Faraday's cup. DC signal are extremely prone to electronic noise and this limits the amount of amplification that the electrometer can offer. By modulating the Faraday's cup signal, a higher amplification electrometer can be used. This will permit the detection of particles at lower concentration, but also require specialized circuit design.
- (d) Another option is to run multiple units of the micro ionizer and mini-DMA in parallel. This increases the number of charged particles per unit time which results in corresponding increases in the electric current at the Faraday's cup. Under this option, the Faraday's cup would have to be modified to accommodate the larger flow rate.
- (e) The micro ionizer and mini-DMA could also be redesigned to accommodate a higher flow rate. Due to the nature of using MEMS technology, this will not significantly increase the footprint of the device. To achieve a threefold increase in the flow rate, the same chip size can be used by increasing the spacing between the electrodes. However, this cannot be done cheaply or easily as the entire microfabrication process needs to be carried out from scratch.
- (f) Finally, it would be useful to increase the capture efficiency of the Faraday's cup. Trapping mesh of different material (stainless steel, copper etc) and of different pore size and density can be experimented with to investigate their respective capture efficiencies under various operating conditions.

Finally, since the MicroAPA is designed from scratch, many of its off-the-shelf components should also be optimized.

Technology Transfer

In 1999, UC Davis formed the Technology Transfer Center, which handles intellectual property for the Davis campus. The center serves as a liaison between the UC Davis campus community and business sectors in the natural, physical, engineering and life sciences. The Center is the first point of contact for UC Davis inventions and technology and streamlines the process of patenting and licensing intellectual property. The Center handles coordinating patent processes, negotiating licensing agreements, and negotiating material transfer agreements. The project team has elected to open source the design documents for the prototype. Screenshots of the web pages have been included in the Appendix and additional material can be found at UC Davis Technology Transfer Office.

The study team coordinated closely with the Technology Transfer Center throughout the project to develop the appropriate business relationships and licensing agreements. A patent was filed on the ionizer. As follow-up to this, members of the research team are also participating in the UC Davis Graduate School of Management's competition "The Little Bang" in February 2007. The Little Bang poster competitions provide an opportunity for undergraduate, graduate and post-doc students to showcase the research and technologies originating in the UC Davis labs. In addition to exploring the commercial impact of their innovations, the winners earn a cash prize and a berth in the Big Bang! semi-finals.

APPENDIX

Screen Shots of Open Sourcing Web Material

Main Page:

ENVIRONMENTAL MONITORING: THE MICRO AIRBORNE PARTICULATE ANALYZER (MicroAPA)

Executive Summary

Executive Summary

Step-by-Step Construction

MicroElectroMechanical Systems (MEMS)

Downloadable Layouts

Vendors List

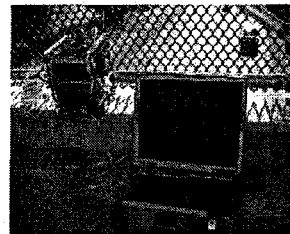
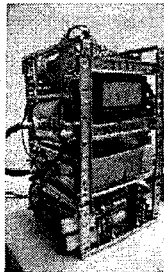
Publications & Patent

Open Source Documents

Other Useful Links

Recent technological advances in hardware design and systems architecture have resulted in a new generation of sensors that are capable of monitoring a range of chemical and physical information. This website provides open source material for the prototype of a new low-cost micro-scale sensor technology that allows real-time measurement of fine particulate matter size distributions. The new sensor element is based on micro electro-mechanical systems (MEMS) technology, which reduces the footprint and the bulk manufacturing cost and coupled with off-the-shelf miniature power supply (both high and low voltages) units, data acquisition modules and air pumps.

The MicroAPA includes a custom designed and fabricated MEMS based ionizer and mini-DMA (separator electrodes), custom designed electrometer and Faraday's cup, as well as a number of off-the-shelf components.



The MicroAPA: Systems Operation Map

By developing new, small footprint, low cost sensors, researchers will be able to better deploy and quantify PM2.5 number distributions in a variety of environments where sampling with conventional instruments is not practical or affordable.

Project Sponsors: The California Air Resources Board, The California Energy Commission

Step by Step Construction:

ENVIRONMENTAL MONITORING: THE MICRO AIRBORNE PARTICULATE ANALYZER (MicroAPA)

Step-by-Step Construction

Executive Summary

Step-by-Step Construction

MicroElectroMechanical Systems (MEMS)

Downloadable Layouts

Vendors List

Publications & Patent

Open Source Documents

Other Useful Links

AIR FLOW PATH

STEP 1: Microfabricate the integrated corona ionizer and separator electrodes and package it. (see MEMS section)

STEP 2: Connect the Sensidyne AAA micro air pump to the inlet of the corona ionizer.

STEP 3: Connect the outlet from the separator electrodes to the inlet of the Faraday's cup.

STEP 4: Exhaust the outlet from the Faraday's cup into OMRON Flowmeter D6F-02A1-110.

ELECTRICAL CONNECTIONS

STEP 1: Connect both the corona ionizer and separator electrodes to output of Picoelectronics HV-DC-DC converters.

STEP 2: Power the Picoelectronics HV-DC-DC converters, Sensidyne Micro air pump and OMRON Flowmeter using a Triangle Research T100MD888 Super PLC board via an non-inverting voltage buffer circuit (standard EE textbook material). Use a relay if necessary if the carrier current gets too large.

STEP 3: Connect the output from the Faraday's cup to the CERMET transimpedance amplifier (see vendor list).

STEP 4: Connect CERMET amplifier output to the ADC (analog to digital) port of the Triangle Research T100MD888 Super PLC.

By developing new, small footprint, low cost sensors, researchers will be able to better deploy and quantify PM2.5 number distributions in a variety of environments where sampling with conventional instruments is not practical or affordable.

Project Sponsors: The California Air Resources Board, The California Energy Commission

MEMs:

ENVIRONMENTAL MONITORING: THE MICRO AIRBORNE PARTICULATE ANALYZER (MicroAPA)

MicroElectroMechanical Systems (MEMS)

Executive Summary

Step-by-Step Construction

MicroElectroMechanical Systems (MEMS)

Downloadable Layouts

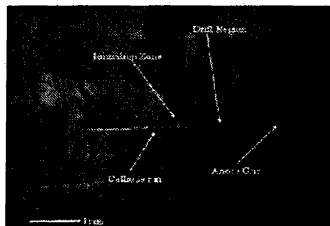
Vendors List

Publications & Patent

Open Source Documents

Other Useful Links

MEMS uses microfabrication techniques, similar to those used to manufacture integrated circuits, to create tiny electro mechanical devices such as car air bag sensors (accelerometers). In the MicroAPA, microfabrication is used to manufacture micro corona ionizer and separator electrodes. The 20 microns wide corona needle is placed precisely between two parallel plates that are 2mm apart.



Fabrication Facility: Northern California Nanofabrication Center (NCNC), Kemper Hall, UC Davis

By developing new, small footprint, low cost sensors, researchers will be able to better deploy and quantify PM2.5 number distributions in a variety of environments where sampling with conventional instruments is not practical or affordable.
Project Sponsors: The California Air Resources Board, The California Energy Commission

Downloadable Layouts:

ENVIRONMENTAL MONITORING: THE MICRO AIRBORNE PARTICULATE ANALYZER (MicroAPA)

Downloadable Layouts

[Executive Summary](#)

[Step-by-Step
Construction](#)

[MicroElectroMechanical
Systems \(MEMS\)](#)

[Downloadable Layouts](#)

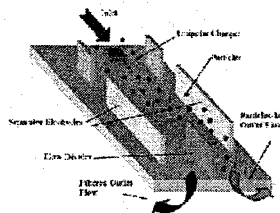
[Vendors List](#)

[Publications & Patent](#)

[Open Source Documents](#)

[Other Useful Links](#)

- [Buffer Circuit Board](#)
- [Ionizer Board](#)
[Free layout editor for designing/viewing
circuit boards](#)
- [Micro Ionizer Fabrication Mask](#)
[Free general purpose layout and design
system editor](#)



By developing new, small footprint, low cost sensors, researchers will be able to better deploy and quantify PM2.5 number distributions in a variety of environments where sampling with conventional instruments is not practical or affordable.

Project Sponsors: [The California Air Resources Board](#), [The California Energy Commission](#)

Vendors List:

ENVIRONMENTAL MONITORING: THE MICRO AIRBORNE PARTICULATE ANALYZER (MicroAPA)

Vendors List

Executive Summary

Step-by-Step Construction

MicroElectroMechanical Systems (MEMS)

Downloadable Layouts

Vendors List

Publications & Patent

Open Source Documents

Other Useful Links

- Micro Air Pump: <http://www.sensidyne.com/>
- Microfabrication Facility: <http://ncnc.engineering.ucdavis.edu/>
- Layout Editor: LAsI <http://members.aol.com/lasicad/>
- Micro Flowmeter: <http://www.components.omron.com/>
- Faraday's Cup: <http://www.baracorp.com/>
- Transimpedance amplifier: Custom Designed
- Printed Circuit Board: <http://www.expresspcb.com/>
- Super PLC: <http://www.tri-plc.com/t100md.htm>
- Relays/Switches/Batteries: Radioshack

By developing new, small footprint, low cost sensors, researchers will be able to better deploy and quantify PM2.5 number distributions in a variety of environments where sampling with conventional instruments is not practical or affordable.
Project Sponsors: The California Air Resources Board, The California Energy Commission

Publications and Patent:

ENVIRONMENTAL MONITORING: THE MICRO AIRBORNE PARTICULATE ANALYZER (MicroAPA)

Publications & Patent

Executive Summary

Step-by-Step Construction

MicroElectroMechanical Systems (MEMS)

Downloadable Layouts

Vendors List

Publications & Patent

Open Source Documents

Other Useful Links

[1] B.L. Chua, Z. Li, D.T. McCormick, W.P. Shih, N.C. Tien, A.S. Wexler, D.A. Niemeier and B. Holmén, "A Unipolar Corona Discharge Microfabricated Ionizer Structure For Gases At Atmospheric Pressure And Composition", Technical Digest 17th IEEE International Conference on Micro Electro Mechanical Systems, Maastrich Netherlands, Jan 25-29 2004, pp 261-264

[2] B. L. Chua, M. Zhang, A.S. Wexler, N.C. Tien, D.A. Niemeier and B.A. Holmen, "Collection of non-gas phase airborne nanoparticles by microfabricated electrostatic precipitator", in Technical Proceedings CANEUS 2004 Conference on Micro-Nano-Technologies, Monterey, (2004), AIAA 2004-6731, pp. 141-149

[3] B. L. Chua, M. Zhang, J.M. Huber, A.S. Wexler, N.C. Tjen, D.A. Niemeier and B.A. Holmen, "A configuration for high flow rate, high efficiency and low pressure loss micromachined active air filtration element for airborne micro-nanoscale particles separation and removal", in Technical Digest 18th IEEE International Conference Micro Electro Mechanical Systems, Miami, FL, USA, 2005, pp 718-721

[4] "Microfabricated device for selectively removing and analyzing airborne particulates from an air stream" US Patent 7098462, 29th August 2006

By developing new, small footprint, low cost sensors, researchers will be able to better deploy and quantify PM2.5 number distributions in a variety of environments where sampling with conventional instruments is not practical or affordable.
Project Sponsors: The California Air Resources Board, The California Energy Commission

Open Source Documents:

ENVIRONMENTAL MONITORING: THE MICRO AIRBORNE PARTICULATE ANALYZER (MicroAPA)

Open Source Documents

[Executive Summary](#)

[Step-by-Step Construction](#)

[MicroElectroMechanical Systems \(MEMS\)](#)

[Downloadable Layouts](#)

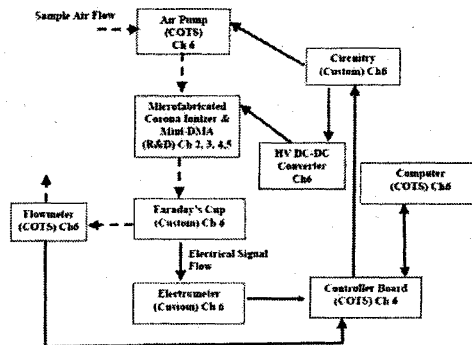
[Vendors List](#)

[Publications & Patent](#)

[Open Source Documents](#)

[Other Useful Links](#)

- Final Report (coming soon)
- Systems Operation Map



By developing new, small footprint, low cost sensors, researchers will be able to better deploy and quantify PM_{2.5} number distributions in a variety of environments where sampling with conventional instruments is not practical or affordable.
Project Sponsors: The California Air Resources Board, The California Energy Commission

Other Useful Links:

ENVIRONMENTAL MONITORING: THE MICRO AIRBORNE PARTICULATE ANALYZER (MicroAPA)

[Executive Summary](#)

[Step-by-Step Construction](#)

[MicroElectroMechanical Systems \(MEMS\)](#)

[Downloadable Layouts](#)

[Vendors List](#)

[Publications & Patent](#)

[Open Source Documents](#)

[Other Useful Links](#)

Other Useful Links

Air Resources Board: <http://www.arb.ca.gov/>

California Energy Com: <http://www.energy.ca.gov/>

TSI: <http://www.tsi.com/>

EPA NCER: <http://es.epa.gov/ncer/>

Free layout editor for designing/viewing circuit board layouts:
<http://www.expresspcb.com/ExpressPCB.htm#Download.htm>

Free general purpose layout and design system editor:
<http://members.aol.com/lasicad/download.htm>

Contacts

[Developers](#)

[B.A. Holmen](#)

[Anthony Wexler](#)

[Norman Tien](#)

[Deb Niemeier](#)

By developing new, small footprint, low cost sensors, researchers will be able to better deploy and quantify PM2.5 number distributions in a variety of environments where sampling with conventional instruments is not practical or affordable.
Project Sponsors: The California Air Resources Board, The California Energy Commission